Journal of Structural Geology 163 (2022) 104721

Contents lists available at ScienceDirect

Journal of Structural Geology

journal homepage: www.elsevier.com/locate/jsg

Olivine-rich veins in high-pressure serpentinites: A far-field paleo-stress snapshot during subduction

Antonio Jabaloy-Sánchez [a,*], Vicente López Sánchez-Vizcaíno [b], José Alberto Padrón-Navarta [c,d], Károly Hidas [e], María Teresa Gómez-Pugnaire [f], Carlos J. Garrido [c]

[a] Departamento de Geodinámica, Universidad de Granada, 18002, Granada, Spain
[b] Departamento de Geología (Unidad Asociada al IACT-CSIC), Universidad de Jaén, 23700, Linares (Jaén), Spain
[c] Instituto Andaluz de Ciencias de la Tierra, CSIC-Universidad de Granada, 18100 Armilla, Granada, Spain
[d] Géosciences Montpellier, University of Montpellier, CNRS, 34095 Montpellier Cedex 05, France
[e] Departamento de Geología y Subsuelo, Project Office in Granada, Centro Nacional Instituto Geológico y Minero de España del CSIC, 18006, Granada, Spain
[f] Departamento de Mineralogía y Petrología, Universidad de Granada, 18002, Granada, Spain

A B S T R A C T

Field observations within the Atg-serpentinite domain of the subducted ultramafic massif from Cerro del Almirez (SE Spain) reveal the existence of two generations of abundant olivine-rich veins formed as open, mixed mode and shear fractures during prograde metamorphism. Type I veins were synchronous with the development of the serpentinite main foliation (S_1) and shearing, whereas Type II veins post-date the S_1 surfaces. These structural relationships indicate that, while the Atg-serpentinites underwent ductile plastic deformation at temperatures of 450°-600 °C and pressures of 0.7–1.7 GPa, they also experienced punctuated brittle behaviour events. The brittle fractures were most likely due to fluid overpressures formed by release of H_2O during the brucite breakdown reaction for the case of Type I veins (2 vol % H_2O) and due to a combination of minor dehydration reactions related to continuous compositional and structural changes in antigorite (0.3 vol % H_2O) for Type II veins. Type II olivine-rich veins were formed by brittle failure in a well-defined paleo-stress field and were not significantly deformed after their formation. Comparison of the principal paleo-stress orientation inferred from Type II veins with those formed at peak metamorphic conditions in the ultramafic rocks at Cerro del Almirez shows a relative switch in the orientation of the maximum and minimum principal paleo-stress axes. These relative changes can be attributed to the cyclic evolution of shear stress, fluid pressure and fault-fracture permeability allowing for stress reversal.

1. Introduction

Hydrated ultramafic rocks (serpentinites) are one of the main sources of subduction zone fluids (e.g. Ulmer and Trommsdorff, 1995; Hacker, 2008). Serpentinite-derived fluids are released at different pressure and temperature conditions through several *quasi*-discontinuous dehydration reactions, namely through the breakdown of brucite and antigorite forming olivine at forearc depths (e.g. Kempf et al., 2020 and references therein), and the terminal breakdown of antigorite forming olivine and orthopyroxene at subarc depths (Ulmer and Trommsdorff, 1999; Padrón-Navarta et al., 2010a). Despite the importance of fluids release on the subduction dynamics and the generation of mechanical instabilities at their corresponding depths, natural observations recording such prograde processes are scarce (e.g. Hoogerduijn Strating and Vissers, 1991; Trommsdorff et al., 1998; Hermann et al., 2000; Padrón-Navarta et al., 2010a, 2011; Healy et al., 2009; Weinberg and Regenauer-Lieb, 2010; Jabaloy-Sánchez et al., 2015; Dilissen et al., 2018; Plümper et al., 2017; Bloch et al., 2018; Kempf et al., 2020). The record of the shallower and colder brucite-breakdown reaction (<1.0 GPa and <450 °C) in serpentinites has been almost invariably linked to vein-related structures (Hoogerduijn Strating and Vissers, 1991; Healy et al., 2009; Plümper et al., 2017; Bloch et al., 2018; Kempf et al., 2020), whereas the deeper and hotter high-pressure terminal antigorite dehydration (>1.5 GPa and ca. 660 °C) shows pervasive replacement patterns with varied textures (Padrón-Navarta et al., 2010b, 2011, 2015; Jabaloy-Sánchez et al., 2015; Dilissen et al., 2018). The low-pressure terminal antigorite dehydration producing olivine and talc (<0.4 GPa and ca. 560 °C) occurs as veins and pervasive transformation of serpentinites (Clément et al., 2019). These previous works have provided important constraints on the contrasting fluid flow mechanisms associated with these dehydration reactions, but the potential role of the far-field stress in controlling the geometry of the structures and eventually dictating the fluid pathways remains poorly understood. This ambiguity is partially due to the time-integrated history of the dehydration-related structures, where brittle and ductile deformation usually alternate at different space- and time-scales, thus obscuring the role of different individual

* Corresponding author.
E-mail address: jabaloy@ugr.es (A. Jabaloy-Sánchez).

https://doi.org/10.1016/j.jsg.2022.104721
Received 29 October 2021; Received in revised form 16 August 2022; Accepted 1 September 2022
Available online 7 September 2022

processes (e.g. Muñoz-Montecinos et al., 2020; Druguet et al., 2021), and to the poorly constrained rheology and parameters controlling fluid-flow at high-pressure subduction zone conditions (Tenthorey and Cox, 2003; Kawano et al., 2011; Gasc et al., 2017; Leclère et al., 2018).

The geometry of olivine-rich veins related to the brucite plus antigorite coupled breakdown reaction has been interpreted as the result of dehydration-induced fracturing (Hoogerduijn Strating and Vissers, 1991; Hermann et al., 2000; Healy et al., 2009) or, more recently, as the consequence of a purely internally-controlled process related to the initial mm-scale chemical heterogeneities of the reacting serpentinite that eventually upscales into a cm-to m-scale fractal geometry network due to channelized fluid flow (Plümper et al., 2017). The latter authors propose the formation of almost monomineralic olivine veins by the following general reaction:

$$Mg_{48}Si_{34}O_{85}(OH)_{62} + 20\ Mg(OH)_2 = 34\ Mg_2SiO_4 + 51\ H_2O \quad (1)$$

antigorite + brucite = olivine + aqueous fluid

However, other parameters such as the high time-integrated fluid/rock ratio and the metasomatic capacity of the percolating fluids (Bucher, 1998; Balashov and Yardley, 1998; Oliver and Bons, 2001; Bons et al., 2012; Marsala and Wagner, 2016) may also play a role other than the merely closed-system isochemical perspective of reaction (1). The structural analysis of vein-related structures in high-pressure serpentinites offers a unique opportunity to investigate the evolution of the far-field stress during prograde subduction, their potential seismogenic imprint and its relationship with ongoing dehydration reactions.

Here we report the results from field observations within one subducted antigorite-serpentinite body from Cerro del Almirez (SE, Spain) that records the formation of olivine-rich veins in prograde serpentinite through reaction (1) in addition to the terminal antigorite breakdown previously studied in this locality (Trommsdorff et al., 1998; Padrón--Navarta et al., 2011 and references therein). We show that the identified generations of olivine-rich veins can be ascribed to an evolution in pressure-temperature and time of extensional, shear and mixed-mode fractures during early subduction until peak metamorphic conditions corresponding to the terminal antigorite breakdown reaction at high-pressure.

2. Geological setting

The Nevado-Filábride Complex (NFC) is the lowest metamorphic complex of the Internal Zones of the Betic Cordillera (SE Spain, Fig. 1a and b). The Iberian provenance of its continental lithological sequence and the E-MORB signature of the metabasites it hosts indicate that the NFC belonged to the Jurassic, extended South Iberian paleomargin, which was subducted below the easterly terranes of the Alborán Domain during the Miocene (Gómez-Pugnaire et al., 2012; Platt et al., 2013; Booth-Rea et al., 2015; Jabaloy-Sánchez et al., 2015, 2019; Dilissen et al., 2018).

The uppermost lithological sequence of the NFC corresponds to the Mulhacén units (Puga et al., 1974, 2002) (Fig. 1b), which underwent Alpine, subduction-related, HP metamorphism at ca. 1.8 GPa and peak temperatures ranging between 550 °C and 680 °C at Early-Middle Miocene times (18-15 Ma, López Sánchez-Vizcaíno et al., 2001; Gómez-Pugnaire et al., 2004, 2012, 2019; Platt et al., 2006). Metaultramafic rocks, that are the subject of this work, are located within and at the top of the Mulhacén units (see Gómez-Pugnaire et al., 2012; Jabaloy-Sánchez et al., 2015; 2019; Padrón-Navarta et al., 2011) (Fig. 1b). They correspond to mantle rock portions exhumed and exposed in the ocean-continent transition of the South Iberian paleomargin (Dilissen et al., 2018; Jabaloy-Sánchez et al., 2019) that were subsequently subducted. Emplacement and coupling in their present position in the NFC sequence took place during fast exhumation shortly after peak metamorphism (López Sánchez-Vizcaíno et al., 2001) due to major shear zones in a transpressional deformation regime (Jabaloy-Sánchez et al., 2015).

The Cerro del Almirez (CdA) massif is the largest outcrop of more than twenty ultramafic rock localities in the NFC (Jabaloy-Sánchez et al., 2019). It occurs as a ca. 400 m thick and ~2.3 km^2 wide tabular body (Jansen, 1936) (Fig. 1c) that was thrust over the metapelites and thin, discontinuous marble bodies of the Mulhacén units (Fig. 1c). The CdA ultramafic massif is composed of several lithologies that uniquely preserve: i) the complete structural and mineralogical record corresponding to the prograde metamorphic evolution during subduction, and ii) the mineral assemblages that attest for the metamorphic peak at eclogite-facies conditions. The subsequent exhumation P-T path is recorded only in small domains with associated late retrograde assemblages: e.g. scarce chrysotile growth in the ultramafic rocks or partial amphibolitization of metarodingites (Laborda-López et al., 2018). Thus, most of the CdA ultramafic massif is formed by rocks equilibrated at the peak P-T conditions.

The main ultramafic rocks are well foliated, ca. 150 m thick, Atg-serpentinite consisting of Atg + Ol + Chl + Mag ± Ilm ± Di ± Tr ± Ti-Chu (Trommsdorff et al., 1998; mineral abbreviations are from Whitney and Evans, 2010) and Ol ± Ti-Chu veins (López Sánchez-Vizcaíno et al., 2005). The modal proportion of diopside and tremolite is highly variable in Atg-serpentinite, thus allowing to define two, Ca-rich and Ca-poor, varieties of this rock type (Padrón-Navarta et al., 2011).

Atg-serpentinite overlies a ca. 70–100 m thick, massive Chl-harzburgite sequence (Fig. 1c), composed by Ol + Opx + Chl + Mag ± Ilm ± Tr ± Ti-Chu (Trommsdorff et al., 1998) and interpreted as the result of Atg-serpentinite dehydration (Trommsdorff et al., 1998) at 680 °C and 1.6–1.9 GPa (Padrón-Navarta et al., 2010b). Peak metamorphic conditions recorded by Chl-harzburgite reached maximum 710 °C, at similar pressures (Padrón-Navarta et al., 2010b). Details about the structural, metamorphic, textural and geochemical evolution of the CdA ultramafic rocks and associated rodingite and ophicarbonate lithologies can be found in Trommsdorff et al. (1998), Padrón-Navarta et al. (2011), Marchesi et al. (2013), Laborda-López et al. (2018), Dilissen et al. (2018), Menzel et al. (2019) and references therein.

3. Subduction- and peak-related structures

In the CdA Atg-serpertinite, the main penetrative planar fabric is a S_1 foliation (Padrón-Navarta et al., 2010b, 2011, 2012; Jabaloy-Sánchez et al., 2015; Dilissen et al., 2018) (Fig. 1c and d), defined by the preferred orientation of antigorite crystals (for the CPO of the antigorite see Padrón-Navarta et al., 2012, 2015, and Dilissen et al., 2018), and both oblate and prolate aggregates of magnetite (Jabaloy-Sánchez et al., 2015; Dilissen et al., 2018). Prolate magnetite aggregates also define a weak L_1 stretching lineation on the S_1 surfaces with a mean N–S trend (Jabaloy-Sánchez et al., 2015; Dilissen et al., 2018). Millimetre-to centimetre-scale shear bands define S–C structures suggesting a simple shear component of the deformation during subduction with a top-to-the-South kinematics (Padrón-Navarta et al., 2012; Jabaloy-Sánchez et al., 2015; Dilissen et al., 2018). The S_1 foliation was formed during the prograde metamorphic path at P-T conditions of 475–630 °C and 1.3–1.9 GPa (Padrón-Navarta et al., 2010a, 2012).

S_1 foliation displays low dips defining a major very open NNE-SSW synform (F_1 fold) plunging with a southward component (Padrón-Navarta et al., 2010b; Jabaloy-Sánchez et al., 2015) (Fig. 1c and d). Upright WNW-ESE very open folds (F_2 folds) deform the hinge and axial surface of F_1 (Padrón-Navarta et al., 2010b). F_1 and F_2 sets of folds are perpendicular to each other and, in the case of a passive layer behaviour, this interference should be a type 1 fold interference, with dome and basin structures (Ramsay, 1962). However, the geological map (Fig. 1c) shows that the axial surface of the F_1 fold is folded, and that a F_2 antiform in the eastern limb of the F_1 synform is replaced laterally by a F_2 synform in the western limb and both F_2 folds plunge in opposite directions on the two limbs of F_1 fold. This interference pattern is

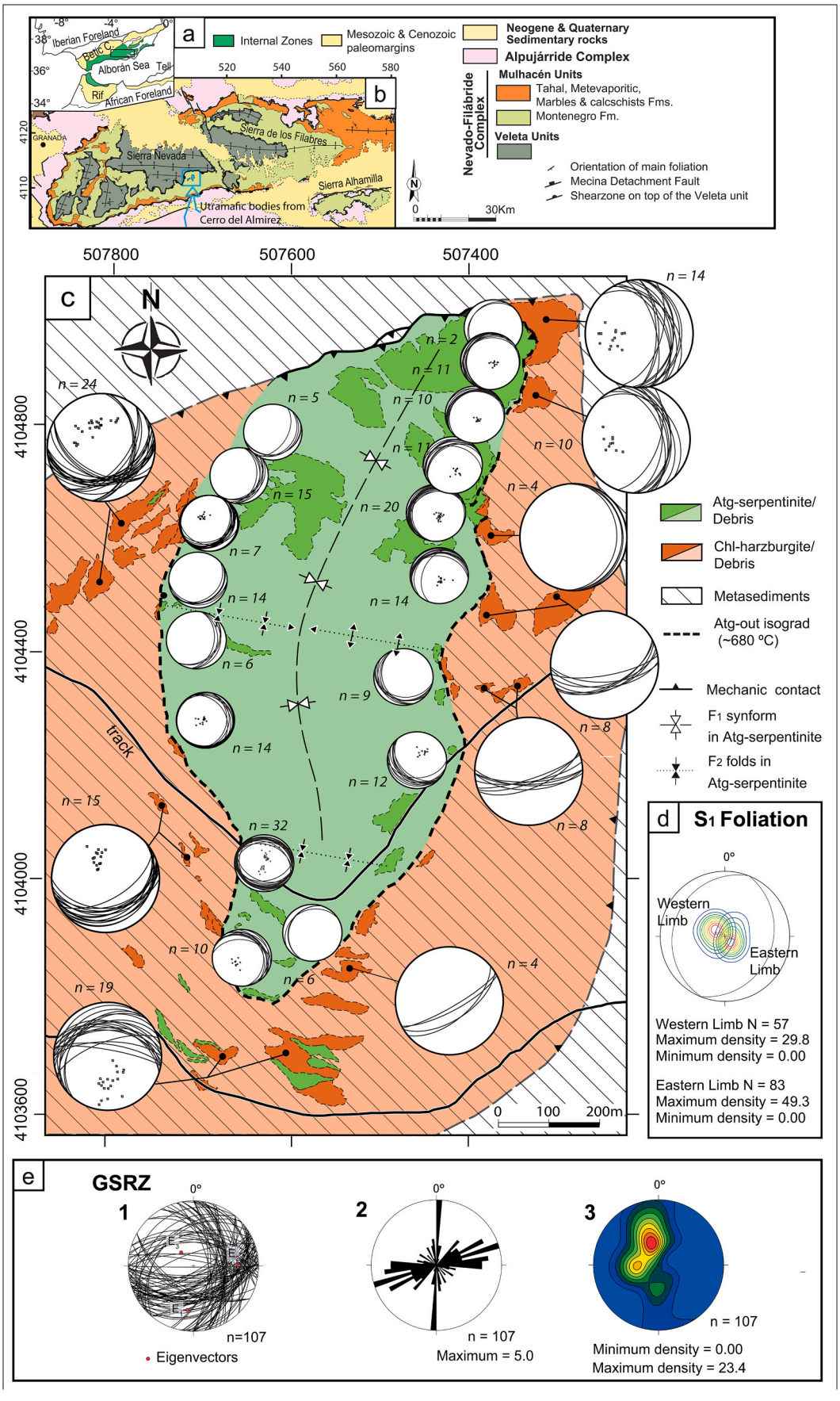

(caption on next page)

Fig. 1. a) Location of the Nevado-Filábride Complex within the Betic-Rif orogenic system. b) Geological map of the Nevado-Filábride Complex in the southwestern Betic Chain. Location of the study area in Fig. 1c is marked with a blue rectangle. c) Geological map of the Cerro del Almirez Massif (geology after Padrón-Navarta et al., 2010b); small stereographic diagrams show the orientation of S_1 foliation in the outcrop (from Padrón-Navarta et al., 2010b), while bigger stereographic diagrams show the orientation of Grain Size Reduction Zones (GSRZ, after Padrón-Navarta et al., 2010b). d) Stereographic projection of the orientation of S_1 foliation in the Cerro del Almirez Massif. e) 1 - Stereographic projection of the orientation of the GSRZ, 2- rose diagram of the strikes of the GSRZ, and 3- density distribution of poles of the GSRZ (data after Padrón-Navarta et al., 2010b and Jabaloy-Sánchez et al., 2015). For interpretation of the references to colour in this figure legend, the reader is referred to the Web version of this article.

characteristic of the mode third of superposed buckling folds (Ghosh et al., 1992), and it clearly indicates that the F_1 folds were older than the F_2 ones and that both F_1 and F_2 folding were due to a buckling process (Ghosh et al., 1992).

S_1 foliation is crosscut by Ol-rich veins (López Sánchez-Vizcaíno et al., 2009; Jabaloy-Sánchez et al., 2015) that are the matter of this work (see section 5). Serpentinite also hosts strongly sheared metarodingite bodies that occur as boudinaged and disrupted layers with two sets of conjugate fractures with low dihedral angles (Laborda-López et al., 2018). This is the same shear event that formed the S_1 foliation and the S–C structures with top-to the-South kinematics before the formation of folds F_1 and F_2. Importantly, metarodingites also register the mineral assemblage sequence corresponding to the prograde P-T path, synkinematic with the HP development of S_1 foliation during subduction (Laborda-López et al., 2018).

The S_1 foliation in the Atg-serpentinites is oblique to the dehydration front defining the transition to massive Chl-harzburgite (Padrón-Navarta et al., 2011; their Fig. 4). Chl-harzburgites display either spinifex-like textures, with large arborescent olivine crystals in a matrix of radial aggregates of acicular orthopyroxene crystals, long chlorite flakes, and aggregates of magnetite, or granofels textures, with coarse granular olivine, intercalated with each other at the meter to tens of meters scale (Padrón-Navarta et al., 2010b; Kahl et al., 2017; Dilissen et al., 2018). Grain size reduction zones (GSRZ) are found to crosscut both the spinifex-like and granofels textures (Padrón-Navarta et al., 2010b) (Fig. 1c, e). They are tabular to irregular zones where a reduction of the olivine grain size occurs from mm-scale to 60–250 μm. GSRZ have very sharp contacts with undeformed Chl-harzburgite domains and are mostly composed of olivine, chlorite, magnetite, and minor tremolite (Padrón-Navarta et al., 2010b). GSRZ have been interpreted to record brittle deformation (microcracking) of the Chl–harzburgite, probably induced by hydrofracturing at peak metamorphic conditions (Padrón--Navarta et al., 2010b) and can be interpreted as high-permeability fluid flow pathways of Atg-dehydration fluids (Padrón-Navarta et al., 2010b). Additionally, structural analysis of GSRZ provided an independent estimate of the orientation of the main paleo-stress axes (σ_1 (188°/30°), σ_2 (091°/32°) and σ_3 (314°/70°)), coeval with the crystallization of Chl-harzburgite (Jabaloy-Sánchez et al., 2015, Fig. 1e).

4. Methods

In this work we have systematically investigated the occurrence of olivine-rich veins, diopside-rich veins and diopside-filled faults, and their structural analysis in the Atg-serpentinite section of the CdA ultramafic massif. We have identified over 50 vein locations and made over 65 orientation measurements (Figs. 2, 4). Paleo-stress analysis was done by using the Faultkin v. 8.1.2 software (Marrett and Allmendinger, 1990; Allmendinger et al., 2012). Thin sections from 25 rock samples were selected for a petrographic description of the veins.

To investigate the phase relationships and the modal fluid proportions in equilibrium with the stable mineral assemblages in Atg-serpentinite during metamorphism, we calculated a P–T pseudosection in the FeO–CaO–MgO–Al_2O_3–SiO_2–H_2O (FCMASH) system using Perple_X 6.9.1 (Connolly, 2009) (Fig. 9). For this calculation, we used the bulk composition of a representative Ca-rich serpentinite of CdA, equivalent to many of those hosting the studied veins (SiO_2: 45.14 wt%; Al_2O_3: 2.48; MgO: 39.00; FeO: 3.87; CaO: 3.46; H_2O: 10.42), the internally consistent thermodynamic database of Holland and Powell (1998) (version 2002) and the compensated Redlich-Kwong (CORK) equation of state (Holland and Powell, 1991) for H_2O–CO_2 fluids. We applied the solid solution models of Holland and Powell (1996) for olivine, orthopyroxene, clinopyroxene, and chlorite, Padrón-Navarta et al. (2013) for antigorite and ideal models for talc, brucite, tremolite, and anthophyllite.

5. Description of the veins and faults

Based on their different mineralogy, size, thickness, orientation, meso and microstructures, and field relation with serpentinites, we have classified olivine-rich veins into two main type sets (Figs. 2–7). Besides, we also describe the associated diopside-rich veins and diopside-filled faults (Fig. 8).

5.1. Type I Ol-rich veins

Type I veins can be better observed on the steep rock cliffs perpendicular to S_1 of the uppermost areas of the Atg-serpentinite section of CdA (Fig. 2a; Fig. 3a–d). They appear as clear brown, tabular, discontinuous veins with lateral continuity ranging from 1 to 10 m and very variable apertures (5–20 cm) (Fig. 3a–c). They mainly consist of massive aggregates of up to 10 cm long tabular olivine megacrysts with a thickness of several millimetres to 4 cm (Fig. 3a–e). In some places, olivine is accompanied by rounded, centimetre long clusters of titanian-clinohumite (Ti-Chu) crystals (López Sánchez-Vizcaíno et al., 2005, 2009) (Fig. 3e). Whitish non-systematic fractures, with several millimetres apertures and filled with prismatic diopside grains (Fig. 3d), crosscut both olivine and Ti-Chu grains. These late whitish diopside veins are lacking in the hosting serpentinites and will be described in the 5.3 subsection.

Type I veins display sharp but strongly convoluted boundaries that cut across the serpentinite S_1 foliation (Fig. 3b). They were in turn affected by shear S–C structures, folds and crenulation (Fig. 3a–f). This resulted in dismembered and boudinaged veins, commonly encompassing crenulated serpentinite fragments (Fig. 3c), as well as in fractured olivine megacrysts (Fig. 3f–h). This deformation post-dated D_1 and produced folding of the veins. In agreement with the reported folding, fracturing and shearing, the strikes and dips of Type I veins do not have a preferred orientation in the field (Fig. 2a and b).

Under the microscope, boundaries of Type I veins with the host serpentinite are sharp and wrapped by the crenulated S_1 foliation (Fig. 3g). Large olivine crystals display systematically oriented and spaced joints with no appreciable apertures on a microscopic scale (Fig. 3h). In some cases, joints define two perpendicular sets, thus resembling cleavage in a mineral that has no cleavage. Xenomorphic, variably-sized opaque mineral inclusions within olivine may also display a preferred orientation linked to that of the joints. When present, large Ti-Chu grains may be partially or completely transformed to olivine + ilmenite breakdown products (López Sánchez-Vizcaíno et al., 2009). Hosting Atg-serpentinites may be similar to any other within this domain (Padrón Navarta et al., 2011). They may contain variable amounts of olivine, diopside, magnetite and sulphides, but are brucite lacking.

5.2. Type II Ol-rich veins

Type II veins are widespread throughout the entire Atg-serpentinite

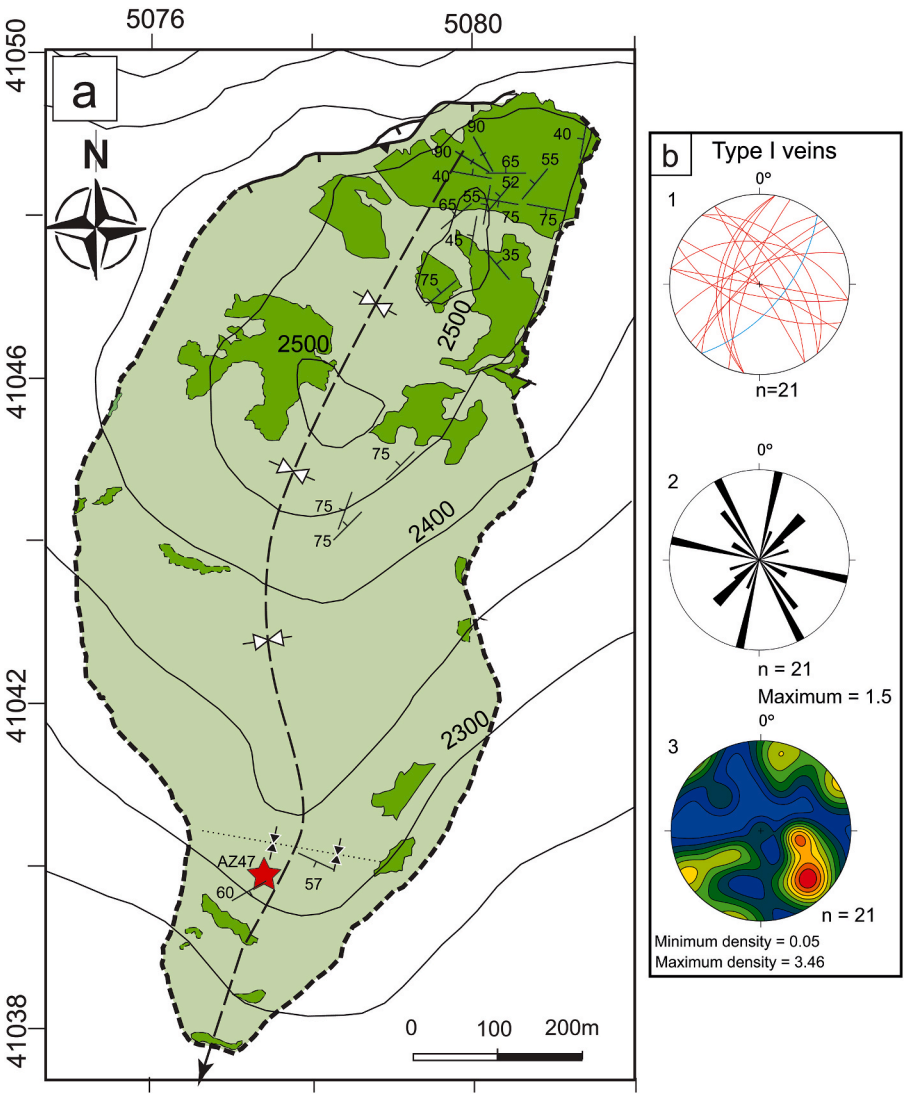

Fig. 2. a) Geological map of the serpentinites within the Cerro del Almirez Massif with the location and orientation of Type I Ol-rich veins. The red star marks the location of AZ47 outcrop with Di faults. b) 1 - Stereographic projection of the orientation of Type I veins: red lines, veins in the eastern limb of F_1 fold, blue line, joint in the western limb of the F_1 fold, 2- rose diagram of the strikes of Type I veins, and 3- density distribution of poles of Type I veins. (For interpretation of the references to colour in this figure legend, the reader is referred to the Web version of this article.)

body (red squares and orientation symbols in Fig. 4). They occur as arrays of red brownish veins with up to 1 m of visible lateral continuity and apertures ranging from several millimetres to 2 cm (Fig. 5a–g). They usually show sharp surfaces at sample scale and cut across the main S_1 foliation (Fig. 5a–e). Curved tips and angular irregularities in their walls matching across the vein are also common (Fig. 5g; see also Jabaloy-Sánchez et al., 2015).

Type II veins arrays can be grouped into one or two sets of systematic planar surfaces (Fig. 4a and b and 5a-c). There are also outcrops with two sets of systematic veins that can be orthogonal, or more frequently, at acute angles defining "conjugate sets" (Fig. 5b and c). Non-systematic veins with curved surfaces are common as well (Fig. 5a) and they can partially brecciate the Atg-serpentinite. Incipiently-developed sets of veinlets are also abundant within the Atg-serpentinite; they appear as very thin (1–2 mm) and less than 3 cm long, irregular veinlets cross-cutting each other (Fig. 5d).

Strikes of the systematic veins indicate two main sets at ca. N100°E and ca. N110°E orientation respectively (Fig. 4b). These ESE-ENW surfaces group into two maxima separated by a dihedral angle of ca. 53°: one set is nearly vertical and the other dips ca. 36° towards NNE. When the spacing of the systematic veins can be measured, it varies between 8 and 50 cm, with a mode of 10–20 cm, and a mean value of 21 cm (Fig. 6). Two minor systematic orthogonal sets are found at ca. N90°E and ca. N0°E, which show high dips, usually between 70° and 90° (Fig. 4b). The orthogonal sets have a joint-system architecture with T shapes (Fig. 5b) (see Dunne and Hanckock, 1994).

Type II veins also comprise shear veins (Fig. 5 e) giving place to: rhomboidal jogs filled with olivine (Fig. 5f), curved extensional faults with wing cracks (Fig. 5g), or the growth of olivine and diopside slickenfibres (Fig. 5h). Besides, some shear veins accommodate sudden changes in the orientation of open veins (Fig. 5e). Some of these shear veins have associated drag folds in the Atg-serpentinite host rock (Jabaloy-Sánchez et al., 2015; their Fig. 6f) and have been used for paleo-stress analysis.

The typical mineral assemblage of Type II veins is composed of Ol-Di-Atg-(Ti-Chu)-(Chl) and clearly differs from that of the almost monomineralic Type I veins. Under the microscope, vein boundaries with the serpentinite display a convoluted, but fuzzy geometry, oblique to the fine-grained antigorite preferential orientation defining foliation (Fig. 7a and b). The fuzzy aspect of the boundaries is due to the presence of flame-like antigorite flakes, parallel to the external foliation, in between the rounded aggregates of olivine grains, all of which is compatible with the crenulation of the Type II veins with axial plane foliation parallel to the hosting serpentinite main foliation. As in the case of Type I veins, no evidence of brucite occurrence in the hosting serpentinite has been detected.

Vein filling mainly consists of granoblastic, and commonly altered, aggregates of olivine grains encompassing hypidiomorphic to

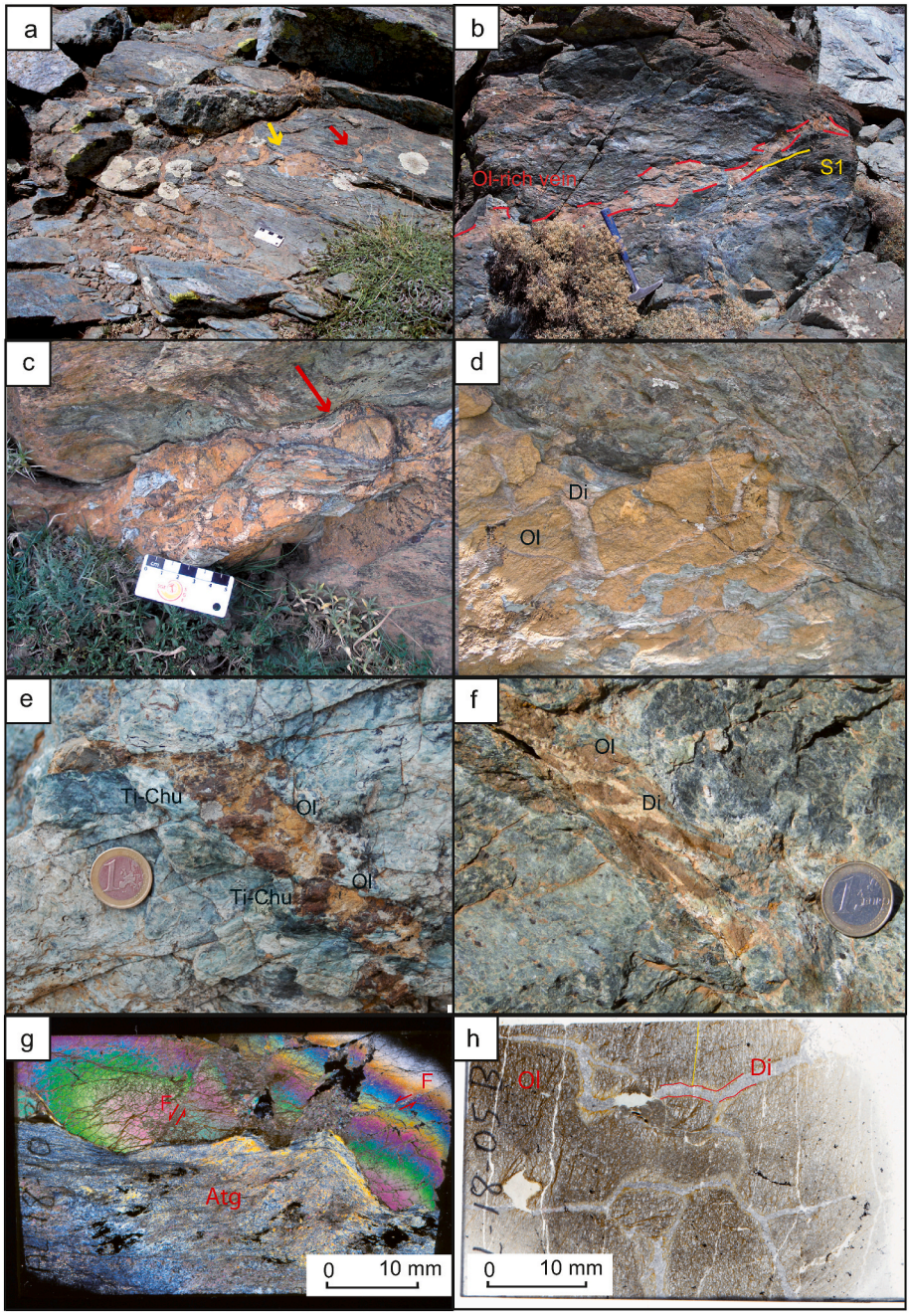

Fig. 3. a) Field occurrence of Type I veins affected by boudins and folds: the yellow arrow marks the neck of a boudin, while the red one marks a folded vein with the S_1 as the axial plane foliation. b) Metre-long, deformed Type I vein with Ol megacrysts. c) Transposed boudin of a Type I olivine-TiChu vein with small polygonal Di veins (whitish mineral) and inclusions of foliated serpentinite fragments. The red arrow marks the neck of a boudin. d) Close view of a Type I vein with Ol megacrysts broken by polygonal Di veins (whitish mineral). Picture is 13 cm wide. e) Type I olivine-TiChu vein with jog geometry; small polygonal Di veins are lacking. f) Sheared Type I vein with olivine and deformed Di veins. g) Microscope view of a faulted Ol megacryst in a Type I vein and the ductile deformed Atg of the wall rock (cross-polarized light). h) Microscope view of an Ol megacryst with systematically oriented and spaced joints and broken by polygonal Di veins (plane polarized light). (For interpretation of the references to colour in this figure legend, the reader is referred to the Web version of this article.)

xenomorphic tabular grains (up to 0.5 mm long) of diopside (Fig. 7c). Xenomorphic aggregates of Ti-Chu grains are frequently associated with olivine (Fig. 4c). Antigorite typically appears as large (up to 0.8 mm long), idiomorphic, randomly oriented and distributed flakes; very different from those of the host serpentinite which are finer-grained and oriented parallel to the S_1 (Fig. 7c). Chlorite flakes are rare near diopside grains. Opaque minerals (i.e., magnetite) are rare within the veins, even if these veins are hosted in serpentinites with very abundant opaque minerals.

At thin section scale, the incipient veinlets appear as roughly oriented but discontinuous strings of fine-grained irregular aggregates (up to 8 mm long) of olivine, diopside and some Ti-Chu and magnetite grains. Aggregates are enclosed by the fine-grained antigorite matrix of host serpentinite and are overgrown by larger, randomly-oriented flakes of antigorite (Fig. 7d).

In few outcrops, whitish, up to 2 cm thick veins are found associated with the Type II veins and also crosscutting the main Atg-serpentinite foliation. At the microscope, they consist of very fine-grained aggregates of strongly crenulated antigorite and granoblastic diopside (vein i in Fig. 7e). Olivine-diopside aggregates like those described in the incipient veins are found to grow on their boundaries with an irregular distribution (boundaries of veinlet i in Fig. 7e). Several generations of mutually crosscutting veins can be seen in Fig. 7e: the Atg-Di vein i is crosscut by Ol-rich veins ii (partially altered to chrysotile), which are in turn crosscut by veinlet iii.

Where the veins and faults contain slickenfibres of olivine and diopside, both minerals appear as centimetre long, parallel-oriented, prismatic, stretched grains with undulose extinction, twin lamellae and regularly spaced inclusion bands (Fig. 7f).

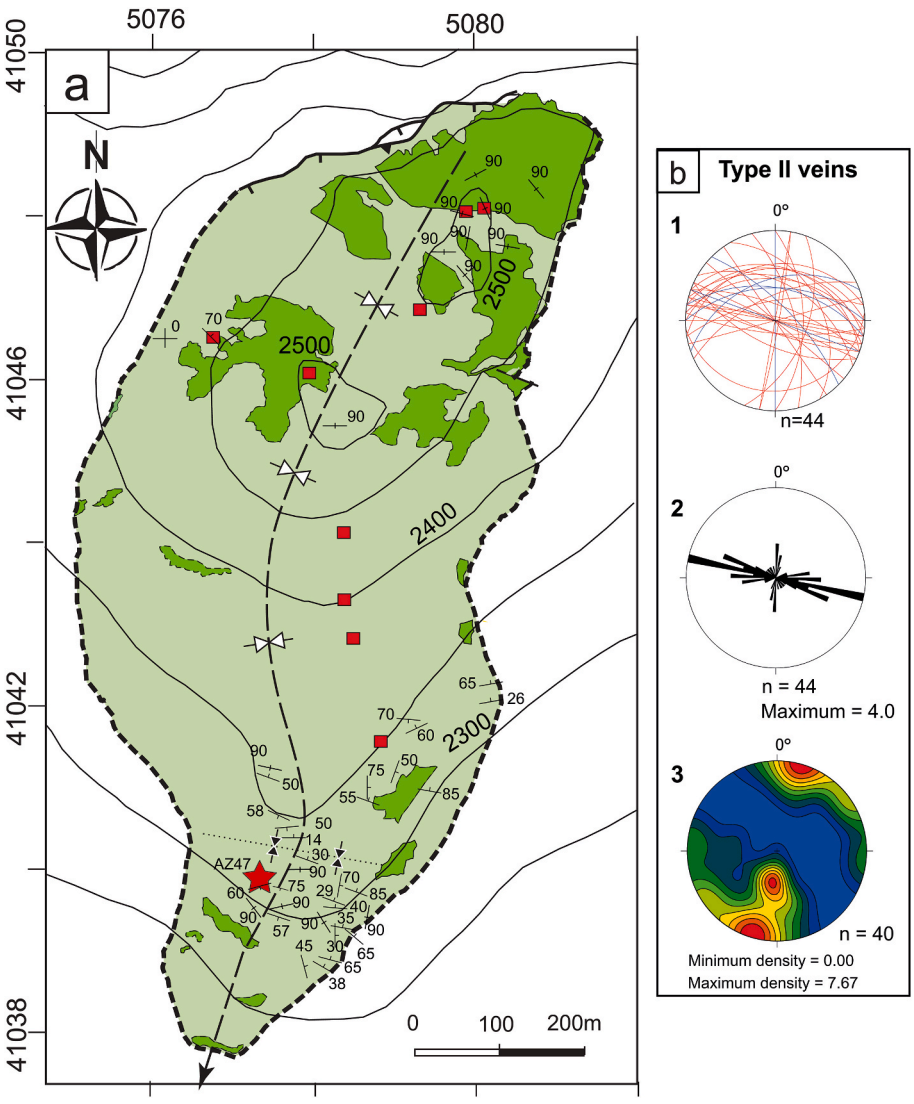

Fig. 4. a) Geological map of the serpentinites within the Cerro del Almirez Massif with the location and orientation of Type II Ol-rich veins. The red squares mark additional outcrops where taking orientation measures was not possible. The red star marks the location of AZ47 outcrop with Di faults. b) 1 - Stereographic projection of the orientation of Type II veins red lines, veins in the eastern limb of F_1 fold, blue lines, joints in the western limb of the F_1 fold, 2-rose diagram of the strikes of Type II veins, and 3-density distribution of poles of Type II veins. (For interpretation of the references to colour in this figure legend, the reader is referred to the Web version of this article.)

5.3. Diopside veins and faults

Fractures filled mainly with prismatic, several millimetres long and 100–200 μm wide diopside aggregates and some fine-grained antigorite occur within the Type I Ol-rich veins (Fig. 3c,d,f,h). These Di veins occur along former olivine-olivine grain boundaries or cut across both olivine and Ti-Chu grains breaking them up into angular fragments of varying size (Fig. 3f). However, diopside-filled fractures have never been found to progress into the serpentinite wall-rock. The polygonal array of Di veins is sheared and folded in several outcrops (Fig. 3f). Thin bands of small inclusions within the diopside are very frequent and define crack seals. A median line is always lacking in these veins. In some places, large prismatic diopside grains are bent and replace olivine.

Other than these veins, metre long faults with slickenfibres of diopside are to be found in one outcrop (AZ47; at UTM coordinates: X = 507736, Y = 4103976, and Z = 2310 (Zone 30S)) of the CdA Atg-serpentinite domain (Figs. 2 and 4 for location, Fig. 8 for the outcrop description). At AZ47 three faults with N–S strikes and different dips can be observed. All three faults are arranged in a reverse left-handed fault system with two splays (Fig. 8), the branch lines being roughly N–S. They cut across a Type I Ol-vein with an aperture of 8 cm and N40°E orientation with a 60° dip towards the SE. Olivine in the vein is also crossed by small non-systematic diopside veins (Fig. 8). The faults also show a reverse off-set of ca. 30 cm for the lower fault and ca. 20 cm for the intermediate one. Close to the fault, the S_1 foliation of the host Atg-serpentinite displays small reverse drag folds. Diopside fibres have grown on the faults surfaces with a 0° to 30° southward pitch. Fibres are well-developed within the extensional jogs and they join the walls of the faults indicating a left-handed reverse movement (Fig. 8). Under the microscope, diopside is prismatic and is associated with antigorite and opaque minerals. In this same outcrop, small, subvertical N–S striking (N0°E) veins filled with diopside are also found.

6. Discussion

Olivine-rich veins have been described in several localities in which serpentinites underwent simultaneous deformation and metamorphism during the Alpine orogeny: Erro-Tobio (; Hoogerduijn Strating and Vissers, 1991; Scambelluri et al., 1991; Plümper et al., 2017; Peters et al., 2020), Val Malenco (Clément et al., 2019), or Piemonte Zone - Zermatt Sass (Groppo and Compagnoni, 2007; Luoni et al., 2018, 2019; Assanelli et al., 2020; Kempf et al., 2020). Detailed structural analysis of rocks and veins has been provided for fully to partially serpentinized peridotites from Erro-Tobio where polyphase ductile structures were used to reconstruct the geometry of the subduction and exhumation cycle (;Hoogerduijn Strating and Vissers, 1991; Hermann et al., 2000). In particular, en-echelon olivine veins from Erro-Tobio locally preserving fibre structures were interpreted as the result of prograde

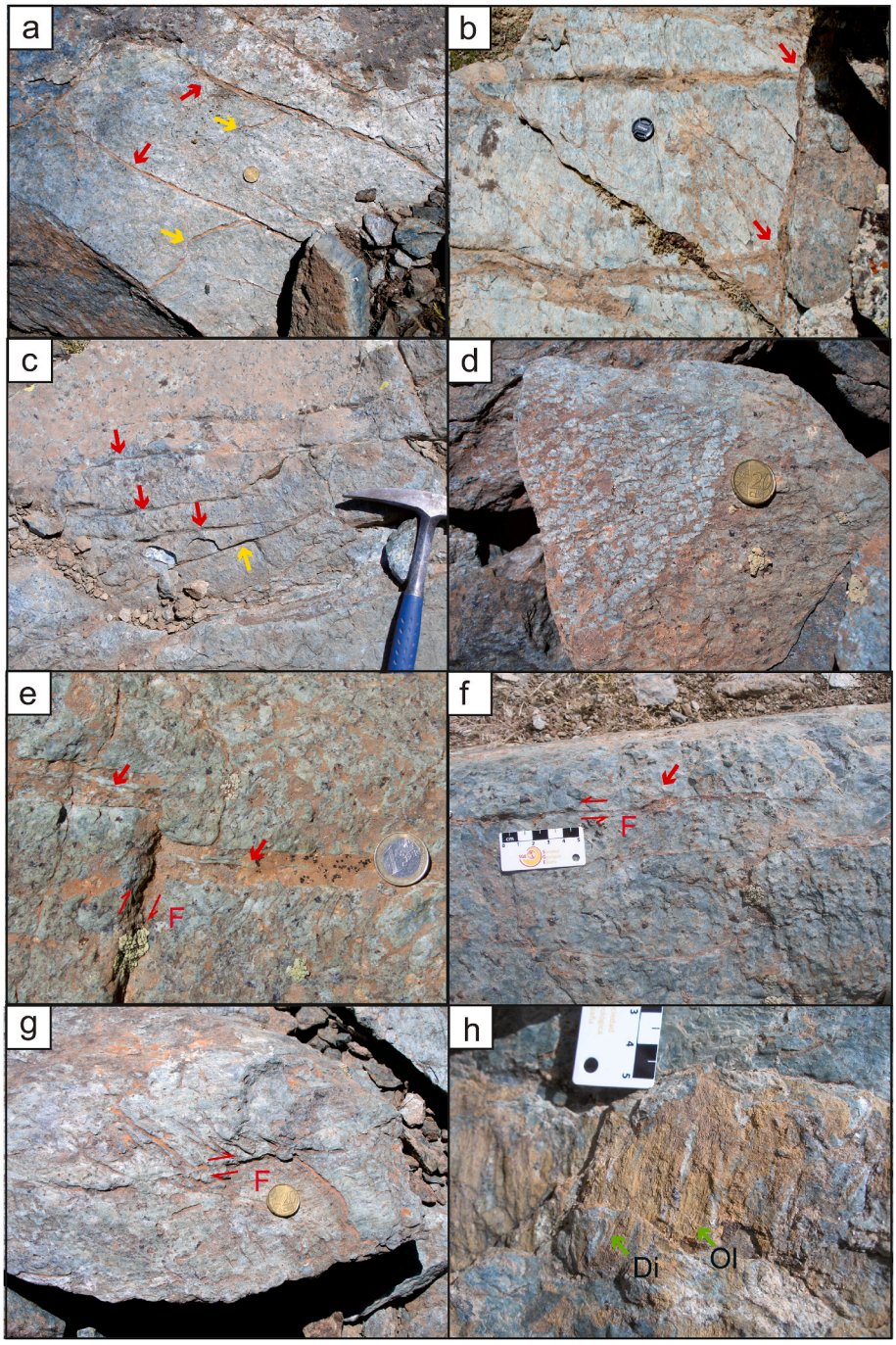

Fig. 5. a) Field occurrence of systematic (red arrows) and non-systematic (yellow arrows) Type II veins. b) Systematic, nearly orthogonal Type II veins with T architecture (red arrows). Systematic oblique veins cut across the outcrop. c) Two sets of systematic Type II veins at small dihedral angles with each other. d) Incipiently-developed sets of veinlets crosscutting each other. e) Two segments of a Ol Type II vein, with fragments of serpentine within the olivine filling, connected by a left-handed shear fracture. f) Type II fault with a jog filled with Ol. g) Type II fault ending in curved extension veins (horse-tail or wing-crack fractures). h) Close front view of the surface of a Type II fault with fibrous Ol (brown) and Di (white) crystals. For interpretation of the references to colour in this figure legend, the reader is referred to the Web version of this article.

subduction at conditions of ca. 1.0–1.5 GPa and 450 °C (Hermann et al., 2000) related to the brucite-breakdown reaction (1), with relict brucite grains being still preserved in the host rock (Scambelluri et al., 1997). Well-developed burial -as opposed to exhumation- (olivine-shear bands) and exhumation (S–C fabrics) structures partially obliterated en-echelon veins, thus precluding a detailed analysis of the relation between the vein-orientation and the main foliation in antigorite serpentinites. On the contrary, the limited development of exhumation related structures in the CdA serpentinites allows us to investigate the mechanisms that led to fracturing and fluid flow through the latest stages of subduction-linked prograde metamorphic evolution. Moreover, because peak-metamorphic conditions were mostly post-kinematic (Padrón-Navarta et al., 2011) the far-field paleo-stress recorded during subduction from vein-orientation analysis can be compared with the estimated orientation of the main paleo-stress directions during the peak-pressure antigorite dehydration event (Jabaloy-Sánchez et al., 2015; Dilissen et al., 2018).

6.1. *Formation of Type I and Type II Ol-rich veins and Di veins and faults*

Two olivine-rich vein types occur in the Atg-serpentinite domain from CdA. According to their different mineral assemblages, grain size of their minerals, and mode of occurrence in the field, it is suggested that they correspond to two vein generations formed during the tectono-metamorphic evolution of serpentinites linked to subduction, but prior to the final dehydration of antigorite producing Chl-harzburgite. Di faults and veins that deform the Ol-rich veins have been also observed.

Type I veins cut across the main S_1 foliation, have the mineral

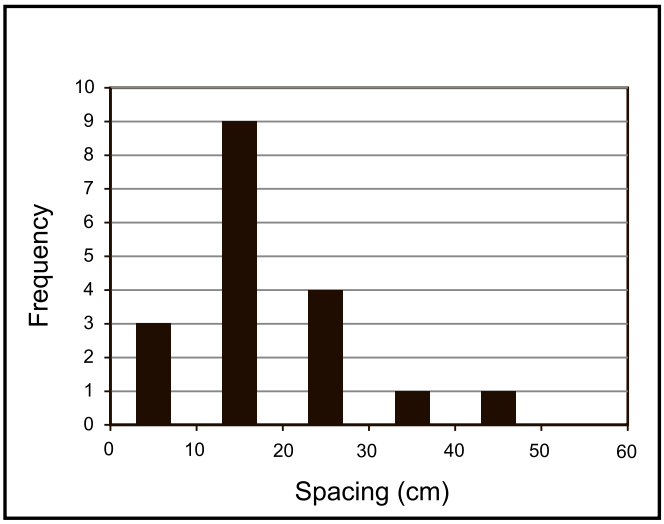

Fig. 6. Diagram of the frequency of the spacing (in cm) in the systematic Type II veins.

assemblage Ol- (Ti-Chu) and are strongly affected by ductile deformation and shearing (c.f. Hermann et al., 2000) that gave place to the loss of lateral continuity and even boudinage of veins, the enclosure of deformed serpentinite fragments, and a very variable orientation, both in strikes and dips, that prevents their original disposition from being set (Fig. 2b).

Type II veins display a more varied mineral composition: Ol-Di-Atg-(Ti-Chu)-(Chl). In the field, they also cut across the Atg-serpentinite S_1 main foliation. However, they appear as systematic veins when observed in planar structures, thus indicating that, in spite of the observed folding on a microscopic scale, they were little affected by post D_1 deformation and they preserve their original relations forming well-defined conjugated sets and preferential orientations that can be compared using S_1 as a reference structural frame (Fig. 4b).

A possible origin for the different orientation of the two vein sets could be that both sets formed at the same stage of fracturing but at different angles to the strain ellipsoid, and, accordingly, subsequent folding only affected some of them (Type I veins) while the rest kept their original orientation (Type II). This hypothesis cannot yet explain the systematic differences between the two vein types in their length, thickness, mineral composition, and mineral grain size (see Table 1 for a summary), or the fact that Type II veins include several sets of differently oriented systematic veins.

Consequently, it can be concluded that the two studied Ol-rich vein types formed at different stages and Type I veins formed before Type II ones and were affected by ductile deformation responsible for the strong mylonitic fabric of Atg-serpentinite (Padrón-Navarta et al., 2012; Jabaloy-Sánchez et al., 2015; Dilissen et al., 2018) formed during ongoing subduction.

The NNE-SSW F_1 and the WNW-ESE F_2 folds developed a mode third of superposed buckling folds (Ghosh et al., 1992). In this context, Type II veins could be interpreted as cross-joints of the NNE-SSW F_1 folds, but they do not record the folding by the F_2 folds. On the other hand, if we consider them to be longitudinal joints of the WNW-ESE F_2 folds, the dips of the two main sets of joints (90° and 36° towards NNE) do not agree with the dips of the limbs of those F_2 folds. Therefore, we suggest that Type II veins could have grown in the last, almost static event described for Atg-serpentinite before the main dehydration event. The attainment of static conditions before the terminal antigorite breakdown is supported by the abnormal high-degree of polysomatic order around m = 17 observed at CdA (Padrón-Navarta et al., 2008, 2011) suggesting temperatures in the range of 450–550 °C at 1.0–2.0 GPa (Mellini et al., 1987; Wunder et al., 2001; Shen et al., 2020). Di faults and veins clearly cut the Type I Ol-rich veins, while we have not observed the relationships between Di structures and Type II veins.

Further constraints on the P-T conditions at which the two Ol-rich

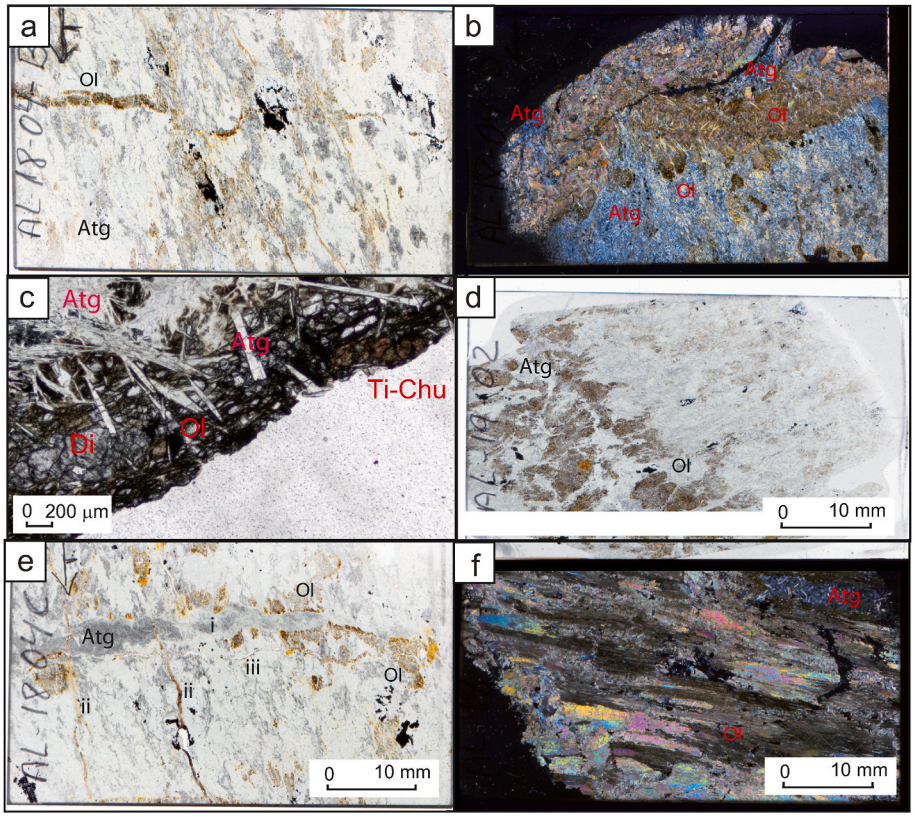

Fig. 7. a) Thin section of a Type II vein crosscutting the main foliation of Atg-serpentinite defined by oriented, dark grey aggregates of dusty clinopyroxene. b) Microscope view of the convoluted wall interface between a Type II vein and the Atg-serpentinite host rock (cross-polarized light). c) Close microscope view of the fuzzy interface between a Type II vein filled with Ol + Atg + Ti-Chu + Di with the Atg-serpentinite host rock. d) Thin section of a so-called incipient vein formed by aligned brownish aggregates of olivine and diopside within Atg. e) Thin section of an Atg and Di-rich vein (i) with brownish olivine aggregates growing in its rims and crosscut by thin olivine veinlets (ii and iii). f) Microscope view of olivine and diopside slickenfibres in a Type II fault (cross-polarized light).

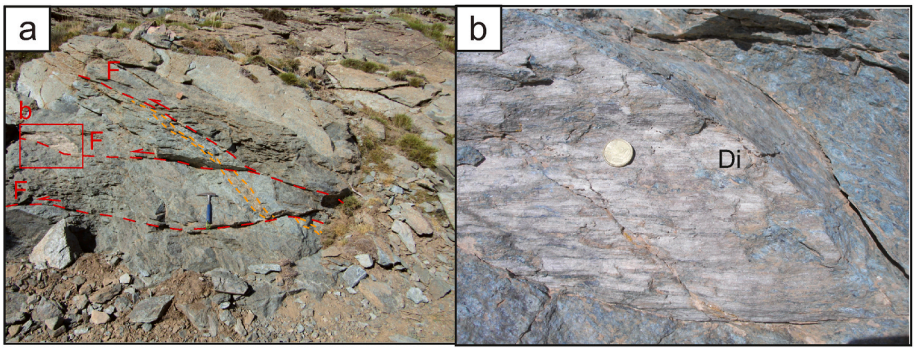

Fig. 8. a) Field view of the AZ47 outcrop with the Di-filled faults (red lines) cutting across a Type I vein (orange lines). The red rectangle marks the location of photograph b. b) Detail of the Di slickenfibres within the fault. For interpretation of the references to colour in this figure legend, the reader is referred to the Web version of this article.

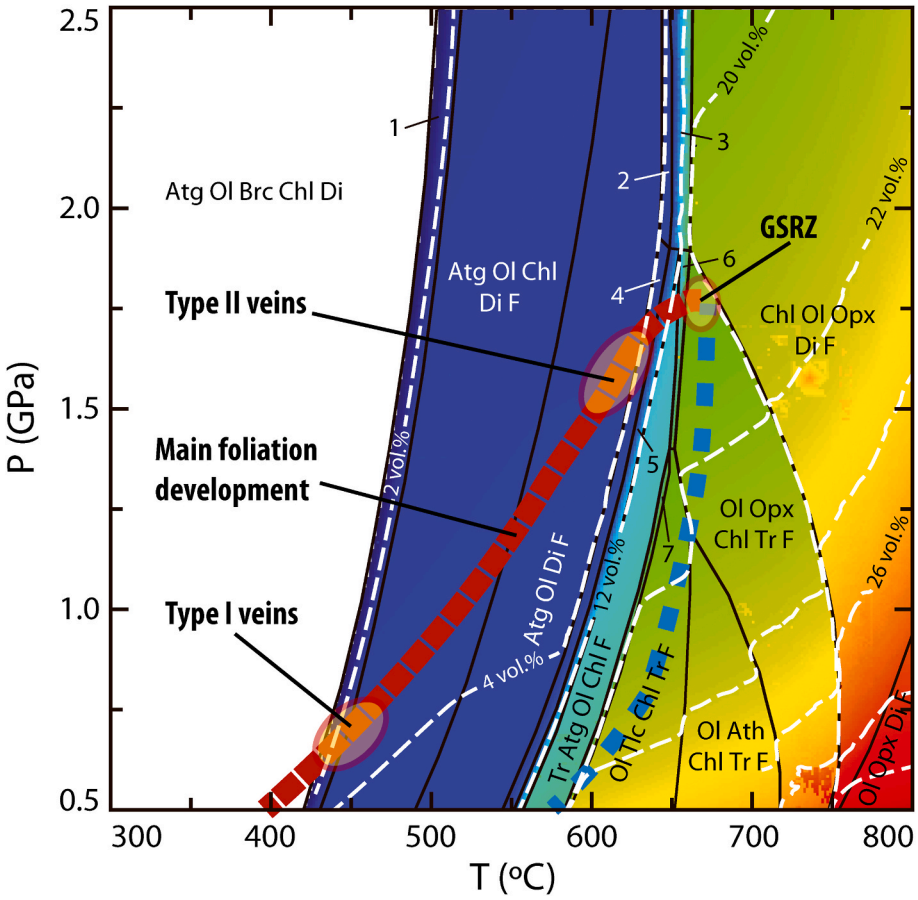

Fig. 9. Calculated metamorphic P-T path for the Cerro del Almirez metaultramafic and metarodingite rocks superposed on a P-T pseudosection calculated for a representative Atg-serpentinite (see Section 4. Methods for details). Thick black lines represent the field limits at which the labelled mineral assemblages are stable (mineral names abbreviations after Whitney and Evans, 2010; F: fluid phase). Background colours show increasing fluid amounts (from blue to red) with temperature due to prograde dehydration reactions as also indicated by dashed white isopleths (vol% H_2O). Shaded ellipsoidal fields show the estimated P-T conditions for the formation of Type I and Type II veins (see text) and GSRZ (Padrón-Navarta et al., 2010b). 1. Atg Ol Brc Chl Di; 2. Atg Ol Opx Di F; 3. Atg Ol Opx Chl Di F; 4. Atg Ol Di Tr F; 5. Atg Ol Chl Di Tr F; 6. Atg Ol Opx Chl Tr F; 7. Atg Ol Tlc Chl Tr F. For interpretation of the references to colour in this figure legend, the reader is referred to the Web version of this article.

vein types developed are supplied by their mineral assemblages. Type I Ol-rich veins are mainly composed of olivine and Ti-Chu. During the prograde evolution of serpentinites, reaction (1) (i.e. brucite and antigorite breakdown at relatively low T, < 450 °C) is a potential mechanism producing olivine growth (Fig. 9). This reaction was also invoked as the explanation of Ti-Chu formation in serpentinites from CdA and other localities (Trommsdorff and Evans, 1980; Hoogerduijn Strating and Vissers, 1991; Scambelluri et al., 1991; López Sánchez-Vizcaíno et al., 2005, 2009; Kempf et al., 2020). Besides, Type II veins display the typical mineral assemblage of Ca-bearing serpentinites (olivine, diopside, Ti-Chu, antigorite and chlorite) in the wide P-T field comprised between the brucite-out and the diopside-out reactions (0.7–1.7 GPa and 450–625 °C; Fig. 9). The specific mechanisms triggering the development of each vein type are discussed below (section 6.3).

6.2. *Causes of brittle behaviour at high-pressure in subducting serpentinites*

As explained, the original field relationships and orientation of Type I veins are partially transposed and modified by later deformation. However, the macroscopic features of Type II veins clearly indicate that they originated due to brittle failure resulting in open-mode fractures (Mode I, Rice, 1968). This is supported by: i) the presence of either one set of systematic planar veins or two sets of orthogonal or conjugate systematic planar veins (Fig. 5b and c); ii) the coherent spacing of those systematic sets (Fig. 6); iii) the coexisting occurrence of non-systematic

Table 1
Summary of the main structural characteristics and mineral assemblages of the studied veins.

	Ol-rich veins		Di-rich veins and faults
	Type I veins	Type II veins	
Mineral assemblage	Ol-Atg-(Ti-Chu)	Ol-Di-Atg-(TiChu)-(Chl)	Di
Lateral continuity	1–10 m	1 cm to 1 m	1 cm to 3 m
Apertures	5–20 cm	5 mm to 2 cm	1 cm–2 cm
Orientation	Very Variable	Two main sets of ESE-ENW systematic veins with vertical 36° NNE dips. Also, non systematic veins.	Non systematic veins cutting minerals in the Type I veins, and left-handed reverse faults
Mesostructures	Dismembered and sheared veins. Strongly convoluted boundaries affected by shear fractures, folds and crenulation. Include crenulated serpentinite fragments	Extensional veins have sharp boundaries with curved tips and angular irregularities matching across the vein. Shear veins have rhomboidal jogs, and wing cracks. Ol and Di slickenfibres can be developed	Di slickenfibres
Microstructures	Fractured olivine megacrysts	Incipient veinlets are roughly oriented, but discontinuous, strings of fine-grained irregular aggregates of Ol, Di and/or Ti-Chu and Mag grains	Prismatic Di growing normal or oblique to the vein boundaries

veins with curved surfaces (Fig. 5a); and iv) the common appearance of curved tips (Fig. 5g). Besides, there are also shear veins, i.e. shear fractures (Fig. 5e) (Modes II or III, Rice, 1968), as evidenced by olivine and diopside slickenfibres (Fig. 5h), horse-tail or wing-crack fractures (Fig. 5g), and the occurrence of rhomboidal jogs (Fig. 5f), and veins with displacements oblique to the surfaces of the fracture (i.e. mixed-mode fractures, Bons et al., 2012) (Fig. 7e).

The presence of extensional, mixed-mode and shear fractures indicates that the Mohr-Griffith-Coulomb failure criterion was at work in these rocks (e.g. Bons et al., 2012, and references therein) during subduction, thus suggesting the fracturing was driven by a brittle-elastic process. This inference is significant given that the mineral assemblage of Type II veins (Ol + Di + Atg + Chl ± TiChu) and the calculated P-T path for the CdA massif (Fig. 9) predict that these veins were formed under high-pressure conditions (1.3–1.8 GPa and 475–625 °C; López Sánchez-Vizcaíno et al., 2009; Padrón-Navarta et al., 2012; Laborda-López et al., 2018), at which brittle failure should be inhibited if a free aqueous fluid phase were absent (see below).

Padrón-Navarta et al. (2012) and Dilissen et al. (2018) observed a strong crystallographic preferred orientation (CPO) of antigorite in serpentinites from CdA based on high resolution electron backscatter diffraction (EBSD) mapping. Based on bulk CPO and intracrystalline misorientation analyses, the activation of dislocation glide through the [100](001) system and a subsidiary glide on the [010](001) system indicate an intracrystalline deformation by dislocation creep (Padrón-Navarta et al., 2012). Although the activation of dissolution-precipitation creep (e.g. Wassmann et al., 2011) and twinning can also influence the formation of the strong CPO (Padrón-Navarta et al., 2012). Based on the fit to the experimental rheological data at high pressure (1.0–4.0 GPa) from Hilairet et al. (2007), the strength of serpentinites deformed by dislocation creep at subduction strain rates of 10^{-14} s^{-1} to 10^{-10} s^{-1} ranges from ca. 7 MPa–70 MPa, respectively. At high pressure and low differential stresses, such as the ones inferred above, the most likely cause of brittle failure has been traditionally attributed to dehydration embrittlement (e.g. Raleigh and Paterson, 1965; but see also Chernak and Hirth, 2011; Gasc et al., 2011, 2017; Ferrand et al., 2017). At lower pressures (0.3 GPa), such as those prevailing at the contact metamorphism of serpentinites in Malenco, tectonic stresses likely related to the intrusion might induce fracturing independently of dehydration (Clément et al., 2019; see also Bucher, 1998). Brittle fractures in cohesive rocks can be formed under high pore fluid pressure at depth, if the relaxation time of the high-fluid pressure is longer than the dissipation time-scale permitted by the intrinsically low permeability at high pressure conditions (e.g., Proctor and Hirth, 2015; de Riese et al., 2020). If the fluid pressure anomaly cannot be dissipated, the increase in the fluid pore pressure reduces the normal stress value and "translates" the Mohr circle towards the left of the Mohr diagram, resulting in the reduction of the strength of the rocks during dehydration (e.g., Raleigh and Paterson, 1965; Jaeger and Cook, 1979). See S1 in the Supplementary material for a more detailed explanation on the conditions for brittle fracturing of the Atg-serpentinites.

For the P-T range established for the possible formation of Type I and II veins in the CdA Atg-serpentinites, the calculated pseudosection indicates that a free fluid phase was always present in the rock (Fig. 9) in amounts ranging from 2 vol% H_2O at the conditions immediately beyond the final brucite breakdown (corresponding to the probable formation conditions of Type I veins) to approximately 6 vol % at the maximum possible temperature allowing the formation of Type II veins (Fig. 9). This upper temperature limit is defined by the growth of tremolite, never found in the veins, at the expense of diopside (narrow fields 4 and 5 in Fig. 9). Besides, in the CdA massif there are also widespread evidences of the activity of fluids in the serpentinite-hosted metarodingite outcrops as well as in their bulk composition (Fe^{3+}/Fe_{total}) and mineral chemistry (Laborda-López et al., 2018, 2020). These data support the presence of a free-fluid phase during most of their prograde subduction history that accounts for their chemical reequilibrium during their deformation and transposition along the S_1 foliation, and for the reduction of the material strength of the rocks during dehydration (e.g., Raleigh and Paterson, 1965; Jaeger and Cook, 1979).

6.3. Fluid-flow along Ol-rich veins

When a crack opens in a fluid-saturated rock, it will be filled with fluid, following local pressure gradients with a rate that is a function of the wall- and host-rock permeability. Dissolved components in the fluid that is diffusing into the fluid-filled fissure can result in the precipitation of vein minerals if there is a substantial drop in solubility due to a change in pressure in the fluid-filled fissure relative to the host (Ramberg, 1952). This is a well-known mechanism explaining the common formation of quartz- or calcite-filled veins in crustal settings (e.g. Bons et al., 2012; de Riese et al., 2020).

For the almost monomineralic, Type I olivine-veins, their growth can be considered synkinematic with the brucite-out reaction, which supplied the necessary MgO-rich aqueous fluids (Fig. 9). The widespread occurrence of Type I veins in CdA and of very similar veins in other localities worldwide (e.g. Luoni et al., 2018, 2019; Assanelli et al., 2020; Hoogerduijn Strating and Vissers, 1991; Scambelluri et al., 1991; Hermann et al., 2000; Kempf et al., 2020) suggests that formation of olivine veins linked to the brucite-out dehydration reaction is a highly efficient process in subduction zones at high-pressure conditions (see also Bloch et al., 2018 for a geophysical expression of such reaction).

Evidences of ductile deformation in the hosting Atg-serpentinite of Type I veins and within the veins themselves (i.e., boudins and folds affecting the Ol-rich bands) can be accounted for by the probable decrease in the rock fluid pore pressure due to the occurrence of several interconnected fractures. This allowed the formation of fluid pathways and, consequently, also fluid flow and drainage from the rock, which

will inhibit brittle failure (section 6.2) and favour ongoing deformation through ductile mechanisms (e.g. Muñoz-Montecinos et al., 2020; Druguet et al., 2021). Once the permeability leading to Type I veins vanishes with time, olivine growth is inhibited resulting in the brittle behaviour of olivine megacrysts at the considered temperatures (see King and Marone, 2012, for the frictional properties of olivine at 400 to 600 °C), thus explaining the formation of the observed faults, joints and disruption along former grain boundaries (Fig. 3).

The formation of a second generation of Ol-rich veins (Type II) implied a new increase in pore fluid pressure until brittle failure conditions were eventually reached again. At the temperature range comprised between the brucite-out and diopside-out (tremolite-in) reactions (Fig. 9) no other major dehydration reactions can be invoked as the source of fluids allowing the generation of veins in serpentinites. A reliable alternative process is the reported change in the antigorite polysome from $m = 17$ to $m = 15$–14 in the Atg-serpentinites from CdA towards the dehydration front (Padrón-Navarta et al., 2008, 2011). This change was accompanied by a decrease in the antigorite Al-content, which in turn entailed the release of minute but definitive amounts of H_2O (0.29 wt%, Padrón-Navarta et al., 2012). These low fluid amounts might have induced the "delayed" embrittlement represented by Type II veins. This process, affecting the Atg-serpentinite domain as a whole, would be consistent with the wider distribution of these veins, their relatively limited development (low lateral continuity and small apertures), and the common occurrence of the so-called "incipient veins". The latter would record the initial stages of vein formation when H_2O-rich fluid escaping from serpentinite began to concentrate in small domains of rock, before being constrained to a well-defined vein, but already giving place to the crystallization of fine-grained, granoblastic aggregates of olivine and diopside (Fig. 7d). The presence of inclusion bands in slickenfibres of elongated olivine crystal grains in shear fractures suggests that those grains experienced "periodic" sealing and fracturing of the crystals, i.e. crack-seal growth (Ramsay, 1980; Ramsay and Huber, 1983, 1987), and confirms their brittle behaviour.

As in the case of Type I veins, the development of Type II ones ceased when they were sealed by the mineral assemblage filling them and fluid flow was precluded. However, in this case they developed during the last stages of ductile deformation of the serpentinite before the final antigorite dehydration in static conditions (see above), which allowed the preservation of their original orientation and other macroscopic features without further deformation. Accordingly, Type II veins offer a unique opportunity to infer the far field paleo-stress regime of serpentinites during subduction, before the metamorphic peak conditions were reached, and the final antigorite dehydration took place (Fig. 9).

6.4. *Far field paleo-stress previous to and during the antigorite dehydration*

During their final emplacement, tectonic units from exhumed paleo-subduction terrains were most probably folded and rotated with respect to their original orientation in the subducting slab. In the following discussion, we will therefore refer to the paleo-stress orientations in the studied rocks in the reference frame defined by their current mutual relationships.

The orientation of the main set of systematic extension Type II veins, with ca. N100°E to N110°E strikes (Fig. 4b), and two minor sets of orthogonal extension veins at ca. N0°E and ca. N90°E strikes, suggests that these fractures formed under a well-defined paleo-stress field. The two sets of the ENE-WSW extension veins with a dihedral angle of ca. 53° can be interpreted as conjugated mixed-mode fractures (see Dunne and Hanckock, 1994). Accordingly, the σ_2 principal stress axis can be located at the intersection of both sets (0° towards N110°E), the σ_1 axis as bisector of the acute dihedral angle (ca. 62° towards N20°E), and σ_3 axis normal to both (ca. 27° towards N200°E) axes (Fig. 10a).

Paleo-stress orientation inferred from Type II systematic extension veins are compared with those determined in other structures in the ultramafic rocks of CdA: i) CPO of Ol and Opx in the Chl-harzburgite (Dilissen et al., 2018, 2021), and ii) GSRZ in the same rock type (Fig. 1e, Padrón-Navarta et al., 2010a; Jabaloy-Sánchez et al., 2015). Agreement is good for the σ_2 axis orientation between both Type II veins and GSRZ, as well as the Y axis of the S_1/L_1 planar-linear fabric of the Atg-serpentinites (Fig. 10a). On the contrary, there is a relative switch between σ_1 and σ_3 as deduced from the veins and GSRZ, but both plot on the XZ plane of the S_1/L_1 planar linear fabric. The orientation of the main paleo-stress axis (σ_1) inferred from the prograde S_1/L_1 fabric (Padrón-Navarta et al., 2012; Dilissen et al., 2018), the GSRZ (Fig. 1f, Padrón-Navarta et al., 2010a; Jabaloy-Sánchez et al., 2015), and the CPO of Ol and Opx in the Chl-harzburgite (Dilissen et al., 2018, 2021) all cluster at ca. 20-45° from the main antigorite foliation. Conversely, the orientation of σ_1 axis inferred from Type II extension veins is located close to the pole of the main Atg-serpentinite foliation plane and thus close to the minimum principal paleo-stress (σ_3) inferred from GSRZ (Fig. 10, see also the pole density contour distribution for Type II veins and GSRZ in Figs. 4b and 1e respectively).

Paleo-stress analysis was applied to the different types of shear surfaces in the Atg-serpentinites: namely, Type II shear veins with their slicken fibres, the boundaries of Type I veins reworked as shear surfaces, and the diopside-filled faults (Fig. 10b). The Linked Bingham Analysis yields the orientation of the strain main axes of the faulted body ($E_1 > E_2 > E_3$) and the stress main axes are deduced from them. All shear surfaces are compatible with a paleo-stress tensor with a σ_3 now dipping ca. 39° towards N139°E, a σ_2 now dipping ca. 13° towards N240°E, and a σ_1 now dipping ca. 48° towards N346°E (Fig. 10b).

The major point here is that two paleo-stress regimes -that determined from Type II extension veins and that resulting from the slip inversion of shear fractures- are mutually incompatible, due to their different axes orientation. We show that only the σ_1 axis determined with the shear surfaces (Fig. 10b) is located close to the σ_1 axis inferred from Type II extension veins (Fig. 10a), but both the σ_2 and σ_3 axes determined with the shear surfaces are at high angles (ca. 40°) of the σ_2 and σ_3 axes from Type II extension veins (Fig. 10a). Furthermore, both paleo-stress axes are also near the σ_3 deduced from GSRZ, and to the pole of the surface of main Atg-serpentinite foliation (Fig. 10a). This fact suggests the existence of two different fracture stages associated to Type II veins: i) one first stage by which Type II extension veins were formed, and ii) a second one responsible for the new shear fractures and the reworking of the Type I vein boundaries as shear surfaces.

An indirect way to consider the relative orientation of the principal stress axes and the subducting slab is to assume that the serpentinite dehydration front defining the transition to massive Chl-harzburgite was roughly parallel to the limits of the slab (e.g. Hacker et al., 2003). Metamorphic peak conditions deduced from the ultramafic rocks (680–710 °C and 1.6–1.9 GPa, Padrón-Navarta et al., 2010a, 2012) point towards a hot subduction zone for the CdA peak metamorphic conditions: i.e., ca. 700 °C at ca. 60 km depth, thus implying a ca. 12 °C/km geothermal gradient. Because the isotherms in a subduction zone are strongly deflected, the mean geothermal gradient is different for the upper and lower plate. Such low geothermal gradient suggests our observations are only related to the lower plate. In their compilation of thermal models for exhumed subducted rocks, Penniston-Dorland et al. (2015) indicate that hot subduction zones with thermal gradients higher than 10 °C/km can depend on one or more of the next factors: a young subducted crust, low convergence rates (probably below 1–2 cm/year), and low dips of the slab (below 30°). Deduced low dips of the slab are probably due, in most cases, to the fact that we can only observe the shallow parts of the slab, as the dip of a subducting slab increases at depths greater than 100 km (Hu and Gurnis, 2020). In Figs. 1, 2 and 4, we can observe that the lower limit of the Atg-serpentinite, i.e. the dehydration front, is a subhorizontal nearly planar surface in its northern part and has E-W strikes and dips ca. 14° towards the south. If we assume that the portion of the dehydration front dipping around 14° south roughly represents the true dip of the slab at 60 km of depth, then

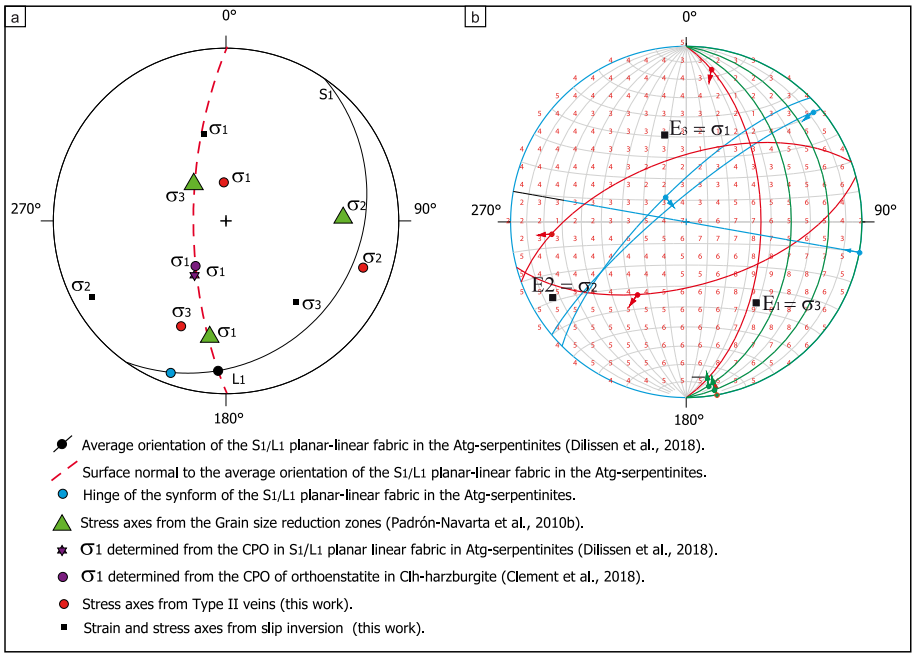

Fig. 10. a) Diagram of the stereographic projection of the different paleo-stresses determined in the ultramafic rocks of the Cerro del Almirez massif. See text for details (Clément et al., 2018). b) Diagram of the Slip inversion method applied on the boundaries of the Type I veins reworked as shear surfaces (blue lines), Type II veins with Ol and Di slickenfibres (red lines), and Di faults (green lines). (For interpretation of the references to colour in this figure legend, the reader is referred to the Web version of this article.)

the dips of the paleo-stresses axes of Fig. 10 can be roughly similar to the dips they had during subduction. Accordingly, the high plunge values of σ_3 axis would indicate a true compression paleo-stress, and the high plunges of σ_1 a true extension paleo-stress (e.g. Zoback, 1992). If these constrains are true, then we have records of a geodynamic setting where the slab sometimes was undergoing extension rather than compression.

The orientation of the Type II extension veins at high angles of the foliation plane differs from other foliation-parallel extension veins in subduction mélanges (Ujiie et al., 2018), although interestingly the switch in orientation between the maximum and minimum principal paleo-stress axes has been also inferred from other subduction-related localities (Cerchiari et al., 2020; Muñoz-Montecinos et al., 2020). Moreover, extension parallel to the slab dip has been observed in actual subduction zones by means of phocal mechanisms of intraslab earthquakes at intermediate depths (e.g. Astiz et al., 1988; Pacheco and Singh, 2010). The intraslab intermediate earthquakes are usually linked to metamorphic dehydration reactions in the subducting slab (Kirby et al., 1996; Hacker et al., 2003). A negative buoyancy of the slab due to increasing resistance of the surrounding mantle or a decrease of the convergence rate should give rise to the extension parallel to the dip of such subducting slab.

One possible model to explain the paleo-stress reversal is that the cyclic evolution of shear stress, fluid pressure and fault-fracture permeability with time along the subduction interface were responsible for the switch in paleo-stress orientation.

As a result of previous discussion, we infer that Type II extension veins record the orientation of the principal paleo-stresses under the last horizontal extensional cycle before the final antigorite dehydration reaction took place. Dehydration most likely happened under horizontal compression conditions, as inferred from the slip inversion of shear fractures, the orientation of GSRZ and CPO of olivine and orthopyroxene in the prograde Chl-harzburgite, thus suggesting that fluid-flow was constrained by the orientation of the former serpentinite foliation planes.

7. Conclusions

The here discussed structures indicate that while the Atg-serpentinites underwent temperatures ranging between 450 °C and 600 °C and pressures between 0.7 and 1.7 GPa (López Sánchez-Vizcaíno et al., 2009; Padrón-Navarta et al., 2012; Laborda-López et al., 2018), they also experienced punctuated brittle behaviour producing two generations of Ol-rich veins. In Type I veins the brittle behaviour was most likely due to the fluid overpressures reached in the rocks by the 4% vol H_2O released during the prograde dehydration reactions at these conditions (Fig. 9). Plastic deformation generated the S_1 foliation during the deformation of the Atg-serpentinites, but the pore pressure of the fluids inhibited the ductile deformation and triggered the formation of the Type I veins, more likely by hydrofracturing. The size of these brittle structures can account for part of the seismicity of a subducting slab at depths ranging between ca. 40 and 60 km related to serpentinites (e.g. Bloch et al., 2018). Plastic deformation continued after the decreasing of the pore pressures and allowed the formation of folds, boudins, and the penetrative joints in the olivine megacrysts.

After the ductile deformation of the Atg-serpentinites ended, Type II Ol-rich veins were formed within the bodies of serpentinites comprised between the Type I veins. The mechanism at work was brittle failure, but in this case a well-defined triaxial paleo-stress field controlled their orientations. Water release was due to a combination of minor dehydration reactions related to continuous compositional and structural changes in antigorite (ca. 0.3 vol % H_2O) for Type II veins. Comparison of the orientation of the principal paleo-stress axes inferred from Type II veins with those formed at peak metamorphic conditions in the Chl-harzburgite affected by GSRZ shows a relative switch in the orientation of the maximum and minimum principal paleo-stress axes. These relative changes can be attributed to the cyclic evolution of shear stress, fluid pressure and fault-fracture permeability that allow for the paleo-stress reversal.

Credit author statement

Antonio Jabaloy-Sánchez: Conceptualization; Data curation; Formal analysis; Funding acquisition; Investigation; Supervision; Validation; Visualization; Writing - original draft. Vicente López Sánchez-Vizcaíno: Conceptualization; Data curation; Formal analysis; Investigation; Methodology; Resources; Software; Supervision; Validation; Visualization; Writing - original draft; Writing - review & editing, Project administration; Funding acquisition José Alberto Padrón-Navarta: Conceptualization; Data curation; Formal analysis Investigation; Methodology; Resources; Software; Supervision; Validation; Investigation;

Methodology; Writing - original draft; Writing - review & editing Károly Hidas: Conceptualization; Investigation; Methodology; Writing - review & editing. María Teresa Gómez-Pugnaire: Investigation; Supervision; Validation; Writing - review & editing. Carlos J. Garrido: Investigation; Supervision; Validation; Project administration; Funding acquisition.

Declaration of competing interest

The authors declare that they have no known competing financial interests or personal relationships that could have appeared to influence the work reported in this paper.

Acknowledgements

Professor John G. Ramsay explored the frontiers of Structural Geology in four books and several seminal articles, in which he essentially worked on how small-scale structures record deformation and displacement, and how these structures can be upscaled to interrogate processes at the orogen scale. In this work we honour Professor John G. Ramsay by studying some small-scale geological structures in the context of subducted lithologies and we discuss how they can be used to infer the orientation of the principal stress directions during subduction in connection with high-pressure fluid flow.

We are grateful to the Sierra Nevada National Park for providing permits for fieldwork and sampling at the Almirez massif. We further acknowledge the editorial handling by D. Grujic and the reviews of two anonymous reviewers, whose comments and constructive criticism helped to improve the manuscript. This work is part of the project DESTINE (PID2019-105192GB-I00) funded by MICIN/AEI/10.13039/501100011033 and the FEDER program "una manera de hacer Europa". It also takes part, without funding, of the scientific activity of research groups RNM-208, RNM-141, RNM-145, RNM-131, and RNM-374 from the Junta de Andalucía. J.A.P.N. acknowledges support from the Ramón y Cajal program (RYC2018-024363-I). Funding for open access charge: Universidad de Granada/ CBUA.

Appendix A. Supplementary data

Supplementary data to this article can be found online at https://doi.org/10.1016/j.jsg.2022.104721.

References

Allmendinger, R.W., Cardozo, N.C., Fisher, D., 2012. Structural Geology Algorithms: Vectors & Tensors. Cambridge University Press, Cambridge, England, p. 289.

Assanelli, M., Luoni, P., Rebay, G., Roda, M., Spalla, M.I., 2020. Tectono-metamorphic evolution of serpentinites from Lanzo Valleys subduction complex (Piemonte-Sesia-Lanzo zone boundary, western Italian Alps). Minerals 10, 985. https://doi.org/10.3390/min10110985.

Astiz, L., Lay, T., Kanamori, H., 1988. Large intermediate-depth earthquakes and the subduction process. Phys. Earth Planet. In. 53, 80–166. https://doi.org/10.1016/0031-9201(88)90138-0.

Balashov, V.N., Yardley, B.W.D., 1998. Modelling metamorphic fluid flow with reaction-compaction-permeability feedbacks. In: American Journal of Science, vol. 298. Yale University, pp. 441–470. https://doi.org/10.2475/ajs.298.6.441.

Bloch, W., John, T., Kummerow, J., Salazar, P., Krüger, O., Shapiro, S., 2018. Watching dehydration: seismic indication for transient fluid pathways in the oceanic mantle of the subducting Nazca slab. G-cubed 19, 3189–3207. https://doi.org/10.1029/2018GC007703.

Bons, P.D., Elburg, M.A., Gomez-Rivas, E., 2012. A review of the formation of tectonic veins and their microstructures. J. Struct. Geol. 43, 33–62. https://doi.org/10.1016/j.jsg.2012.07.005.

Booth-Rea, G., Martínez-Martínez, J.M., Giaconia, F., 2015. Continental subduction, intracrustal shortening, and coeval upper-crustal extension: PT evolution of subducted south Iberian paleomargin metapelites (Betics, SE Spain). Tectonophysics 663, 122–139. https://doi.org/10.1016/j.tecto.2015.08.036.

Bucher, K., 1998. Growth mechanisms of metasomatic reaction veins in dolomite marbles from the Bergell Alps. Mineral. Petrol. 63, 151–171. https://doi.org/10.1007/BF01164149.

Cerchiari, A., Remitti, F., Mittempergher, S., Festa, A., Lugli, F., Cipriani, A., 2020. Cyclical variations of fluid sources and stress state in a shallow megathrust-zone mélange. J. Geol. Soc. London. 177, 647–659. https://doi.org/10.1144/jgs2019-072.

Chernak, L.J., Hirth, G., 2011. Syndeformational antigorite dehydration produces stable fault slip. Geol. 39, 847–850. https://doi.org/10.1130/G31919.1.

Clément, M., Padrón-Navarta, J.A., Tommasi, A., 2019. Interplay between fluid extraction mechanisms and antigorite dehydration reactions (val Malenco, Italian Alps). J. Petrol. 60, 1935–1962. https://doi.org/10.1093/petrology/egz058.

Clément, M., Padrón-Navarta, J.A., Tommasi, A., Mainprice, D., 2018. Non-hydrostatic stress field orientation inferred from orthopyroxene (Pbca) to low-clinoenstatite (P21/c) inversion in partially dehydrated serpentinites. Am. Mineral. 103, 993–1001. https://doi.org/10.2138/am-2018-6362.

Connolly, J.A.D., 2009. The geodynamic equation of state: what and how. G-cubed 10, Q10014. https://doi.org/10.1029/2009GC002540.

de Riese, T., Bons, P.D., Gómez-Rivas, E., Sachau, T., 2020. Interaction between Crustal-Scale Darcy and Hydrofracture Fluid Transport: A Numerical Study. https://doi.org/10.1155/2020/8891801. Geofluids 891801.

Dilissen, N., Hidas, K., Garrido, C.J., Kahl, W.-A., López Sánchez-Vizcaíno, V., Padrón-Navarta, J.A., 2018. Textural evolution during high-pressure dehydration of serpentinite to peridotite and its relation to stress orientations and kinematics of subducting slabs: insights from the Almirez ultramafic massif. Lithos 320–321, 470–489. https://doi.org/10.1016/j.lithos.2018.09.033.

Dilissen, N., Hidas, K., Garrido, C.J., López Sánchez-Vizcaíno, V., Kahl, W.-A., 2021. Morphological transition during prograde olivine growth formed by high-pressure dehydration of antigorite-serpentinite to chlorite-harzburgite in a subduction setting. Lithos 382–383, 105949. https://doi.org/10.1016/j.lithos.2020.105949.

Druguet, E., Czeck, D.M., Carreras, J., 2021. Fluid-assisted localized embrittlement in an overall ductile fold-and-shear belt: a case study from Cap de Creus. J. Struct. Geol. 153, 104460 https://doi.org/10.1016/j.jsg.2021.104460.

Dunne, W.M., Hanckock, P.L., 1994. Palaeostress analysis of small-scale brittle structures. In: Hancock, P.L. (Ed.), Continental Deformation. Pergamon Press, pp. 101–120.

Ferrand, T.P., Hilairet, N., Incel, S., Deldicque, D., Labrousse, L., Gasc, J., Renner, J., Wang, Y., Green II, H.W., Schubnel, A., 2017. Dehydration-driven stress transfer triggers intermediate-depth earthquakes. Nat. Commun. 8, 15247 https://doi.org/10.1038/ncomms15247.

Gasc, J., Schubnel, A., Brunet, F., Guillon, S., Mueller, H.-J., Lathe, C., 2011. Simultaneous acoustic emissions monitoring and synchrotron X-ray diffraction at high pressure and temperature: calibration and application to serpentinite dehydration. Phys. Earth Planet. In. 189, 121–133. https://doi.org/10.1016/j.pepi.2011.08.003.

Gasc, J., Hilairet, N., Yu, T., Ferrand, T., Schubnel, A., Wang, Y., 2017. Faulting of natural serpentinite: implications for intermediate-depth seismicity. Earth Planet Sci. Lett. 474, 138–147. https://doi.org/10.1016/j.epsl.2017.06.016.

Ghosh, S.K., Mandal, N., Khan, D., Deb, S.K., 1992. Modes of superposed buckling in single layers controlled by initial tightness of early folds. J. Struct. Geol. 14, 381–394.

Gómez-Pugnaire, M.T., Galindo-Zaldívar, J., Rubatto, D., González-Lodeiro, F., López Sánchez-Vizcaíno, V., Jabaloy, A., 2004. A reinterpretation of the Nevado-Filábride and Al Complex (Betic Cordillera): field, petrography and U-Pb ages from orthogneisses western Sierra Nevada, S Spain). Schweiz. mineral. petrogr. Mitt. 84, 303–322. https://doi.org/10.5169/seals-63751.

Gómez-Pugnaire, M.T., Rubatto, D., Fernández-Soler, J.M., Jabaloy, A., López Sánchez-Vizcaíno, V., González-Lodeiro, F., Galindo-Zaldívar, J., Padrón-Navarta, J.A., 2012. U-Pb geochronology of Nevado–Filábride gneisses: evidence for the Variscan nature of the deepest Betic complex (SE Spain). Lithos 146–147, 93–111. https://doi.org/10.1016/j.lithos.2012.03.027.

Gómez-Pugnaire, M.T., Nieto, F., Abad, I., Velilla, N., Garrido, C.J., Acosta-Vigil, A., Barich, A., Hidas, K., López Sánchez-Vizcaíno, V., 2019. Alpine metamorphism in the betic internal zones. In: Quesada, C., Oliveira, J. (Eds.), The Geology of Iberia: A Geodynamic Approach. 2, Regional Geology Reviews. Springer, Cham, pp. 519–544. https://doi.org/10.1007/978-3-030-11295-0_13.

Groppo, C., Compagnoni, R., 2007. Metamorphic veins from the serpentinites of the Piemonte Zone, western Alps, Italy: a review. Period. Mineral. 76, 127–153. https://doi.org/10.2451/2007PM0021.

Hacker, B.R., 2008. H_2O subduction beyond arcs. G-cubed 9, Q03001. https://doi.org/10.1029/2007GC001707.

Hacker, B.R., Peacock, S.M., Abers, G.A., Holloway, S.D., 2003. Subduction factory -2. Are intermediate-depth earthquakes in subducting slabs linked to dehydration? J. Geophys. Res. Solid Earth 108 (ISI), 000181799800003. https://doi.org/10.1029/2001jb001129.

Healy, D., Reddy, S.M., Timms, N.E., Gray, E.M., Brovarone, A.V., 2009. Trench-parallel fast axes of seismic anisotropy due to fluid-filled cracks in subducting slabs. Earth Planet Sci. Lett. 283 (1–4), 75–86. https://doi.org/10.1016/j.epsl.2009.03.037.

Hermann, J., Müntener, O., Scambelluri, M., 2000. The importance of serpentinite mylonites for subduction and exhumation of oceanic crust. Tectonophysics 327, 225–238. https://doi.org/10.1016/S0040-1951(00)00171-2.

Hilairet, N., Reynard, B., Wang, Y., Daniel, I., Sebastien, M., Norimasa, N., Sylvain, P., 2007. High-pressure creep of serpentine, interseismic deformation, and initiation of subduction. Science 318, 1910–1913. https://doi.org/10.1126/science.1148494.

Holland, T., Powell, R., 1991. A Compensated-Redlich-Kwong (CORK) equation for volumes and fugacities of CO_2 and H_2O in the range 1 bar to 50 kbar and 100–1600°C. Contrib. Mineral. Petrol. 109, 265–273.

Holland, T., Powell, R., 1996. Thermodynamics of order-disorder in minerals. 2. Symmetric formalism applied to solid solutions. Am. Mineral. 81, 1425–1437.

Holland, T.J.B., Powell, R., 1998. An internally consistent thermodynamic data set for phases of petrological interest. J. Metamorph. Geol. 16, 309–343. https://doi.org/10.1111/j.1525-1314.1998.00140.x.

Hoogerduijn Strating, E., Vissers, R.L.M., 1991. Dehydration-induced fracturing of eclogite-facies peridotites: implications for the mechanical behaviour of subducting oceanic lithosphere. Tectonophysics 200, 187–198. https://doi.org/10.1016/0040-1951(91)90014-J.

Hu, J., Gurnis, M., 2020. Subduction duration and slab dip. G-cubed 21, e2019GC008862. https://doi.org/10.1029/2019GC008862.

Jabaloy-Sánchez, A., Gómez-Pugnaire, M.T., Padrón-Navarta, J.A., López Sánchez-Vizcaíno, V., Garrido, C.J., 2015. Subduction- and exhumation-related structures preserved in metaserpentinites and associated metasediments from the Nevado–Filábride Complex (Betic Cordillera, SE Spain). Tectonophysics 644–645, 40–57. https://doi.org/10.1016/j.tecto.2014.12.022.

Jabaloy-Sánchez, A., Martín-Algarra, A., Padrón-Navarta, J.A., Martín-Martín, M., Gómez-Pugnaire, M.T., López Sánchez-Vizcaíno, V., Garrido, C.J., 2019. Lithological successions of the internal zones and flysch trough units of the betic chain. In: Quesada, C., Oliveira, J. (Eds.), The Geology of Iberia: A Geodynamic Approach, Regional Geology Reviews, vol. 3. Springer, Cham, pp. 377–432. https://doi.org/10.1007/978-3-030-11295-0_8.

Jaeger, J.C., Cook, N.G.W., 1979. Fundamentals of Rock Mechanics, third ed. Chapman & Hall, London.

Jansen, H., 1936. The geology of Sierra de Baza and adjacent areas of the Sierra Nevada and Sierra de los Filabres. Ph.D. thesis, Vrije Univ., Amsterdam, Netherlands.

Kahl, W.-A., Dilissen, N., Hidas, K., Garrido, C.J., López Sánchez-Vizcaíno, V., Román-Alpiste, M.J., 2017. 3-D microstructure of olivine in complex geological materials reconstructed by correlative X-rayμ-CT and EBSD analyses. J. Microsc. 268, 193–207. https://doi.org/10.1111/jmi.12598.

Kawano, S., Katayama, I., Okazaki, K., 2011. Permeability anisotropy of serpentinite and fluid pathways in a subduction zone. Geol. 39, 939–942. https://doi.org/10.1130/G32173.1.

Kempf, E.D., Hermann, J., Reusser, E., Baumgartner, L.P., Lanari, P., 2020. The role of the antigorite + brucite to olivine reaction in subducted serpentinites (Zermatt, Switzerland). Swiss J. Geosci. 113, 16. https://doi.org/10.1186/s00015-020-00368-0.

King, D.S.H., Marone, C., 2012. Frictional properties of olivine at high temperature with applications to the strength and dynamics of the oceanic lithosphere. J. Geophys. Res. 117, B12203 https://doi.org/10.1029/2012JB009511.

Kirby, S.H., Stein, S., Okal, E.A., Rubie, D.C., 1996. Metastable mantle phase transformations and deep earthquakes in subducting oceanic lithosphere. Rev. Geophys. 34 (2), 261–306. https://doi.org/10.1029/96RG01050.

Laborda-López, C., López Sánchez-Vizcaíno, V., Marchesi, C., Gómez-Pugnaire, M.T., Garrido, C.J., Jabaloy-Sánchez, A., Padrón-Navarta, J.A., Hidas, K., 2018. High-P metamorphism of rodingites during serpentinite dehydration (Cerro del Almirez, Southern Spain): implications for the redox state in subduction zones. J. Metamorph. Geol. 36 (9), 1141–1173. https://doi.org/10.1111/jmg.12440.

Laborda-López, C., Marchesi, C., López Sánchez-Vizcaíno, V., Gómez-Pugnaire, M.T., Dale, C.W., Jabaloy-Sánchez, A., Padrón-Navarta, J.A., Román-Alpiste, M.J., Garrido, C.J., 2020. Geochemical evolution of rodingites during subduction: insights from Cerro del Almirez (southern Spain). Lithos 370–371, 105639. https://doi.org/10.1016/j.lithos.2020.105639.

Leclère, H., Faulkner, D., Llana-Fúnez, S., Bedford, J., Wheeler, J., 2018. Reaction fronts, permeability and fluid pressure development during dehydration reactions. Earth Planet Sci. Lett. 496, 227–237. https://doi.org/10.1016/j.epsl.2018.05.005.

López Sánchez-Vizcaíno, V., Gómez-Pugnaire, M.T., Garrido, C.J., Padrón-Navarta, J.A., Mellini, M., 2009. Breakdown mechanisms of titanclinohumite in antigorite serpentinite (Cerro del Almirez massif, S. Spain): a petrological and TEM study. Lithos 107 (3), 216–226. https://doi.org/10.1016/j.lithos.2008.10.008.

López Sánchez-Vizcaíno, V., Rubatto, D., Gómez-Pugnaire, M.T., Trommsdorff, V., Müntener, O., 2001. Middle Miocene high-pressure metamorphism and fast exhumation of the Nevado-Filábride Complex, SE Spain. Terra. Nova 13, 327–332. https://doi.org/10.1046/j.1365-3121.2001.00354.x.

López Sánchez-Vizcaíno, V., Trommsdorff, V., Gómez-Pugnaire, M.T., Garrido, C.J., Müntener, O., Connolly, J.A.D., 2005. Petrology of titanian clinohumite and olivine at the high-pressure breakdown of antigorite serpentinite to chlorite harzburgite (Almirez Massif, S. Spain). Contrib. Mineral. Petrol. 149, 627–646. https://doi.org/10.1007/s00410-005-0678-3.

Luoni, P., Rebay, G., Spalla, M.I., Zanonim, D., 2018. UHP Ti-chondrodite in the Zermatt-Saas serpentinite: constraints on a new tectonic scenario. Am. Mineral. 103, 1002–1005. https://doi.org/10.2138/am-2018-6460.

Luoni, P., Zanoni, D., Rebay, G., Spalla, M.I., 2019. Deformation history of ultra high-pressure ophiolitic serpentinites in the Zermatt-saas zone, Creton, upper Valtournanche (Aosta valley, western Alps). Ofioliti 44, 111–123. https://doi.org/10.4454/ofioliti.v44i2.468.

Marchesi, C., Garrido, C.J., Padron-Navarta, J.A., Lopez Sanchez-Vizcaino, V., Gomez-Pugnaire, M.T., 2013. Element mobility from seafloor serpentinization to high-pressure dehydration of antigorite in subducted serpentinite: insights from the Cerro del Almirez ultramafic massif (southern Spain). Lithos 178, 128–142. https://doi.org/10.1016/j.lithos.2012.11.025.

Marrett, R.A., Allmendinger, R.W., 1990. Kinematic analysis of fault-slip data. J. Struct. Geol. 12, 973–986. https://doi.org/10.1016/0191-8141(90)90093-E.

Marsala, A., Wagner, T., 2016. Mass transfer and fluid evolution in late-metamorphic veins, Rhenish Massif (Germany): insight from alteration geochemistry and fluid-mineral equilibria modelling. Mineral. Petrol. 110, 515–545. https://doi.org/10.1007/s00710-016-0424-8.

Mellini, M., Trommsdorff, V., Compagnoni, R., 1987. Antigorite polysomatism - behavior during progressive metamorphism. Contrib. Mineral. Petrol. 97, 147–155.

Menzel, M.D., Garrido, C.J., López Sánchez-Vizcaíno, V., Hidas, K., Marchesi, C., 2019. Subduction metamorphism of serpentinite-hosted carbonates beyond antigorite-serpentinite dehydration (Nevado-Filabride Complex, Spain). J. Metamorph. Geol. 37, 681–715. https://doi.org/10.1111/jmg.12481.

Muñoz-Montecinos, J., Angiboust, S., Cambeses, A., García-Casco, A., 2020. Multiple veining in a paleo–accretionary wedge: the metamorphic rock record of prograde dehydration and transient high pore-fluid pressures along the subduction interface (Western Series, central Chile). Geosphere 16, 765–786. https://doi.org/10.1130/GES02227.1.

Oliver, N.H.S., Bons, P.D., 2001. Mechanisms of fluid flow and fluid-rock interaction in fossil metamorphic hydrothermal systems inferred from vein-wall rock patterns, geometry and microstructure. Geofluids 1, 137–162. https://doi.org/10.1046/j.1468-8123.2001.00013.x.

Pacheco, J.F., Singh, S.K., 2010. Seismicity and state of stress in Guerrero segment of the Mexican subduction zone. J. Geophys. Res. 115, B01303 https://doi.org/10.1029/2009JB006453.

Padrón-Navarta, J.A., Hermann, J., Garrido, C.J., López Sánchez-Vizcaíno, V., Gómez-Pugnaire, M.T., 2010a. An experimental investigation of antigorite dehydration in natural silica-enriched serpentinite. Contrib. Mineral. Petrol. 159, 25–42. https://doi.org/10.1007/s00410-009-0414-5.

Padrón-Navarta, J.A., López Sánchez-Vizcaíno, V., Garrido, C.J., Gómez-Pugnaire, M.T., 2011. Metamorphic Record of High-pressure Dehydration of Antigorite Serpentinite to Chlorite Harzburgite in a Subduction Setting (Cerro del Almirez Ultramafic Massif, Nevado-Filábride Complex, S. Spain). J. Petrol. 52 (10), 2047–2078. https://doi.org/10.1093/petrology/egr039.

Padrón-Navarta, J.A., López Sánchez-Vizcaíno, V., Garrido, C.J., Gómez-Pugnaire, M.T., Jabaloy, A., Capitani, G., Mellini, M., 2008. Highly ordered antigorite from Cerro del Almirez HP–HT serpentinites, SE Spain. Contrib. Mineral. Petrol. 156, 679–688. https://doi.org/10.1007/s00410-008-0309-x.

Padrón-Navarta, J.A., López Sánchez-Vizcaíno, V., Hermann, J., Connolly, J.A.D., Garrido, C.J., Gómez-Pugnaire, M.T., Marchesi, C., 2013. Tschermak's substitution in antigorite and consequences for phase relations and water liberation in high-grade serpentinites. Lithos 178, 186–196. https://doi.org/10.1016/j.lithos.2013.02.001.

Padrón-Navarta, J.A., Tommasi, A., Garrido, C.J., López Sánchez-Vizcaíno, V., 2012. Plastic deformation and development of antigorite crystal preferred orientation in high-pressure serpentinites. Earth Planet Sci. Lett. 349–350, 75–86. https://doi.org/10.1016/j.epsl.2012.06.049.

Padrón-Navarta, J.A., Tommasi, A., Garrido, C.J., López Sánchez-Vizcaíno, V., Gómez-Pugnaire, M.T., Jabaloy, A., Vauchez, A.M., 2010b. Fluid transfer into the wedge controlled by high-pressure hydrofracturing in the cold top-slab mantle. Earth Planet Sci. Lett. 297, 271–286. https://doi.org/10.1016/j.epsl.2010.06.029.

Padrón-Navarta, J.A., Tommasi, A., Garrido, C.J., Mainprice, D., 2015. On topotaxy and compaction during antigorite and chlorite dehydration: an experimental and natural study. Contrib. Mineral. Petrol. 169 (4), 35. https://doi.org/10.1007/s00410-015-1129-4.

Penniston-Dorland, S.C., Kohn, M.J., Manning, C.E., 2015. The global range of subduction zone thermal structures from exhumed blueschists and eclogites: rocks are hotter than models. Earth Planet Sci. Lett. 428, 243–254. https://doi.org/10.1016/j.epsl.2015.07.031.

Peters, D., Pettke, T., John, T., Scambelluri, M., 2020. The role of brucite in water and element cycling during serpentinite subduction – insights from Erro Tobbio (Liguria, Italy). Lithos 360–361, 105431. https://doi.org/10.1016/j.lithos.2020.105431.

Platt, J.P., Anczkiewicz, R., Soto, J.I., Kelley, S.P., Thirlwall, M., 2006. Early Miocene continental subduction and rapid exhumation in the western Mediterranean. Geol. 34, 981–984. https://doi.org/10.1130/G22801A.1.

Platt, J.P., Behr, W.M., Johanesen, K., Williams, J.R., 2013. The Betic-Rif arc and its orogenic Hinterland: a review. Annu. Rev. Earth Planet Sci. 41 (14) https://doi.org/10.1146/annurev-earth-050212-123951, 1-14.45.

Plümper, O., John, T., Podladchikov, Y.Y., Vrijmoed, J.C., Scambelluri, M., 2017. Fluid escape from subduction zones controlled by channel-forming reactive porosity. Nat. Geosci. 10, 150–156. https://doi.org/10.1038/ngeo2865.

Proctor, B., Hirth, G., 2015. Role of pore fluid pressure on transient strength changes and fabric development during serpentine dehydration at mantle conditions: implications for subduction-zone seismicity. Earth Planet Sci. Lett. 421, 1–12. https://doi.org/10.1016/j.epsl.2015.03.040.

Puga, E., Díaz De Federico, A., Fontbote, J.M., 1974. Sobre la individualización y sistematización de las unidades profundas de la Zona Bética. Estud. Geol. 30, 543–548.

Puga, E., Díaz de Federico, A., Nieto, J.M., 2002. Tectonostratigraphic subdivision and petrological characterisation of the deepest complexes of the Betic zone: a review. Geodin. Acta 15, 23–43. https://doi.org/10.1080/09853111.2002.10510737.

Raleigh, C.B., Paterson, M.S., 1965. Experimental deformation of serpentinite and its tectonic implications. J. geophys. Res. American Geophysical Union 70, 3965–3985. https://doi.org/10.1029/JZ070i016p03965.

Ramberg, H., 1952. A study of veins in Caledonian rocks around Trondheim Fjord, Norway. Nor. Geol., Tidsskr. 41, 1–44.

Ramsay, J.G., 1962. The geometry and mechanics of formation of "similar" type folds. J. Geol. 70, 309–327.

Ramsay, J.G., 1980. The crack-seal mechanism of rock deformation. Nature 284, 135–139. https://doi.org/10.1038/284135a0.

Ramsay, J.G., Huber, M.I., 1983. The Techniques of Modern Structural Geology, 1: Strain Analysis. Academic Press, London.

Ramsay, J.G., Huber, M.I., 1987. The Techniques of Modern Structural Geology, 2: Folds and Fractures. Academic Press, London.

Rice, J.R., 1968. Mathematical analysis in the mechanics of fracture. In: Fracture, Liebowitz H. (Ed.), II, 191-311. Academic Press, New York.

Scambelluri, M., Strating, E.H.H., Piccardo, G.B., Vissers, R.L.M., Rampone, E., 1991. Alpine olivine-bearing and titanian clinohumite-bearing assemblages in the Erro Tobbio peridotite (Voltri-Massif, Nw Italy). J. Metamorph. Geol. 9, 79–91.

Scambelluri, M., Piccardo, G.B., Philippot, P., Robbiano, A., Negretti, L., 1997. High salinity fluid inclusions formed from recycled seawater in deeply subducted alpine serpentinite. Earth Planet Sci. Lett. 148, 485–500.

Shen, T.T., Zhang, C., Chen, J., Hermann, J., Zhang, L.F., Padrón-Navarta, J.A., Chen, L., Xu, J., Yang, J., 2020. Changes in the cell parameters of antigorite close to its dehydration reaction at subduction zone conditions. Am. Mineral. 105, 569–582. https://doi.org/10.2138/am-2020-7159.

Tenthorey, E., Cox, S.F., 2003. Reaction-enhanced permeability during serpentinite dehydration. Geol. 31, 921–924. https://doi.org/10.1130/G19724.1.

Trommsdorff, V., Evans, B.W., 1980. Titanian hydroxyl-clinohumite formation and breakdown in antigorite rocks (Malenco, Italy). Contrib. Mineral. Petrol. 72, 229–242.

Trommsdorff, V., López Sánchez-Vizcaíno, V., Gómez-Pugnaire, M.T., Müntener, O., 1998. High pressure breakdown of antigorite to spinifex-textured olivine and orthopyroxene, SE Spain. Contrib. Mineral. Petrol. 132, 139–148. https://doi.org/10.1007/s004100050412.

Ujiie, K., Saishu, H., Fagereng, Å., Nishiyama, N., Otsubo, M., Masuyama, H., Kagi, H., 2018. An explanation of episodic tremor and slow slip constrained by crack-seal veins and Viscous shear in subduction mélange. Geophys. Res. Lett. 45, 5371–5379. https://doi.org/10.1029/2018GL078374.

Ulmer, P., Trommsdorff, V., 1995. Serpentine stability to mantle depths and subduction-related magmatism. Science 268, 58–861.

Ulmer, P., Trommsdorff, V., 1999. Phase relations of hydrous mantle subducting to 300 km. In: Fei, Y., Bertka, C.M., Mysen, B.O. (Eds.), Mantle Petrology: Field Observations and High Pressure Experimentation. Special Publication No. 6. The Geochemical Society, Houston, pp. 259–281.

Wassmann, S., Stöckhert, B., Trepmann, C.A., 2011. Dissolution precipitation creep versus crystalline plasticity in high-pressure metamorphic serpentinites. Geological Society, London, Special Publications 360, 129–149. https://doi.org/10.1144/SP360.8.

Weinberg, R.F., Regenauer-Lieb, K., 2010. Ductile fractures and magma migration from source. Geol. 38 (4), 363–366. https://doi.org/10.1130/G30482.1.

Whitney, D.L., Evans, B.W., 2010. Abbreviations for names of rock-forming minerals. Am. Mineral. 95, 185–187. https://doi.org/10.2138/am.2010.3371.

Wunder, B., Wirth, R., Gottschalk, M., 2001. Antigorite: pressure and temperature dependence of polysomatism and water content. Eur. J. Mineral 13, 485–495. https://doi.org/10.1127/0935-1221/2001/0013-0485.

Zoback, M.L., 1992. First- and second-order patterns of stress in the lithosphere: the World stress map project. J. Geophys. Res. 97 (B8), 11703–11728. https://doi.org/10.1029/92JB00132.